Article

Not peer-reviewed version

# Effects of HFMI Treatment on The Boron-Alloyed Austenite Medium-Manganese Steel 140Mn6Cr3TiB Deposit: Enhanced Wear Resistance Induced by Heterogeneous Microstructure

Bohdan Trembach , Bohdan Mordyuk * , Michal Krbata , Pavlo Openko , Vadim Zakiev , Vladyslav Shyvaniuk , Tetyana Vladimirova , Mykola Skoryk , Oleksii Kolomiitsev , Vadym Krykun , Yuliia Musairova , Olga Gyrka

Posted Date: 8 June 2026

doi: 10.20944/preprints202606.0435.v1

Keywords: hardfacing; middle-manganese steel; high-frequency mechanical impact; heterogeneous microstructure; martensite; nanoindentation; hardness; scratch test; wear resistance

 doi:10.20944/preprints202606.0435.v1



*Article*

# Effects of HFMI Treatment on The Boron-Alloyed Austenite Medium-Manganese Steel 140Mn6Cr3TiB Deposit: Enhanced Wear Resistance Induced by Heterogeneous Microstructure

**Bohdan Trembach [1], Bohdan Mordyuk [2,3,*], Michal Krbata [4], Pavlo Openko [5], Vadim Zakiev [6], Vladyslav Shyvaniuk [2], Tetyana Vladimirova [2], Mykola Skoryk [2], Oleksii Kolomiitsev [7], Vadym Krykun [8], Yuliia Musairova [9] and Olga Gyrka [10]**

[1] Chief Designer Department of Mining and Press-and-Forging Equipment, Private Joint Stock Company "Novokramatorsky Mashinostroitelny Zavod", Kyiv, 04070, Ukraine
[2] G.V. Kurdyumov Institute for Metal Physics of the NAS of Ukraine, 36, Academician Vernadsky Blvd., Kyiv, 03142, Ukraine
[3] E.O. Paton Electric Welding Institute, NAS of Ukraine, 11, Kazymyr Malevych St. Kyiv, 03150, Ukraine
[4] Faculty of Special Technology, Alexander Dubcek University of Trenčín, 911 06 Trenčín, Slovakia
[5] Deputy Dean for Academic Affairs – Head of the Academic Office, Ivan Kozhedub Kharkiv National Air Force University, Kharkiv, 61045, Ukraine
[6] State University «Kyiv Aviation Institute», 1, Lubomyra Huzara Ave, Kyiv, 03058, Ukraine
[7] Department of the Air Force, Ivan Kozhedub Kharkiv National Air Force University, Kharkiv, 61045, Ukraine
[8] Scientific Research Laboratory, Ivan Kozhedub Kharkiv National Air Force University, Kharkiv, 61045, Ukraine
[9] Scientific Research Department, Ivan Kozhedub Kharkiv National Air Force University, 61023 Kharkiv, Ukraine
[10] Department of commodity science, customs and quality management, Lviv University of Trade and Economics
* Correspondence: mordyuk@imp.kiev.ua; Tel.: +38-044-442-0521

**Abstract**

This paper analyses the microstructure and properties of the titanium- and boron-alloyed high-carbon medium-manganese 140Mn6Cr3TiB steel deposit before and after high-frequency mechanical impact (HFMI) treatment. Nanoindentation revealed a distinct correlation between the phase composition and the deformation behaviour. The heterogeneous nature of the steel creates a "shield-and-buffer" effect, where the hard eutectic framework resists penetration and tough matrix prevents brittle failure. The synergistic interaction between the phases, i.e., the high hardness of boride-carbide phases with the high fracture toughness of the manganese-rich austenite, maintains a high tolerance to abrasion damage of the deposit. The HFMI treatment results in the formation of the strain-induced ε- and α'-martensites (~66% and 3–6%, respectively), a significant grains/crystallites refinement (down to 31–54 nm), and dislocation density (~$2.2*10^{13}$–$5.1*10^{13}$ $cm^{-2}$), which support essential hardening from $HV_{0.2}$ = 5.17 GPa to $HV_{0.2}$ ≈ 7.8 GPa. The HFMI treatment regime (load = 100 N, amplitude = 10 μm, and HFMI time = 60 s) was found to be optimal, which leads to the enhancement in wear resistance of 140Mn6Cr3TiB steel deposit that manifests itself by the decrease of the wear volume by ~4 times from 15.2 $μm^3$ to 3.9 $μm^3$ and in the decrease in the scratch track depths by ~30% (from ~0.52 μm to ~0.37 μm) in comparison with the initial deposit. The HFMI-hardening changed the wear mechanism of high-carbon medium-manganese titanium and boron-alloyed 140Mn6Cr3TiB steel hardfacing to the ploughing mechanism instead of the 'wedge/pile-ups' formation in the initial deposit. The obtained results confirm good efficiency and prospects of the medium-manganese steel

 doi:10.20944/preprints202606.0435.v1



hardfacing followed by the finishing HFMI treatment in the production of protective deposits of enhanced wear resistance and prolonged operation life.

**Keywords:** hardfacing; middle-manganese steel; high-frequency mechanical impact; heterogeneous microstructure; martensite; nanoindentation; hardness; scratch test; wear resistance

## 1. Introduction

Hardening and restoration of worn surfaces are effective technologies that increase service life, reduce operating costs, and improve the reliability of machines and equipment. [1–4]. Hardfacing technologies are widely used in various economic sectors: mining industry [5–8], building equipment [9], agricultural machinery [10–13], oil and gas industry [14,15], railway transport [16–20], heavy industry [21–23], automotive industry [24–28], etc. Machine working units and their parts are subject to various types of wear: abrasive, corrosive, friction (fretting, adhesion, fatigue, polishing), thermal, impact (two-body impact, erosion, cavitation) wear and various combinations of them, for example, tribocorrosive, impact-abrasive, etc. [29]. Abrasive wear causes the greatest damage, but in most cases, it is not pure and acts in conjunction with other types of wear (impact, corrosion, thermal) [30]. This complex issue requires specialists and scientists studying tribology, as well as the development of new materials and coatings, the improvement of existing ones, or the introduction of new testing methods. Such a complex problem requires the improvement of existing testing methods or the introduction of new ones by specialists and scientists studying tribology or developing new materials and coatings.

In the mining and construction industries, as well as in railway engineering, one of the important types of wear is impact-abrasive wear [31–33]. To reduce the degree of impact-abrasive wear, high-manganese steel [34] is traditionally used due to its ability to quickly harden on the surface when exposed to significant impact loads or contact stresses. However, low yield strength and insufficient work hardening rate under low and medium stress conditions are significant disadvantages of this material [35,36]. To increase the service life of mining equipment components, modified medium-manganese austenitic steels (MMAS) were developed [37,38]. MMAS steels typically contain from 5 to 10 wt% Mn. MMAS alloys are effective over a wider range of deformations, unlike classical Hadfield steel, which requires extreme mechanical stresses to activate hardening [39,40]. MMAS alloys have a unique balance of strength and ductility, which is achieved due to the specific nature of strain hardening [41,42]. At low and moderate loads, their hardening ability increases by 60–120% (up to 700 HV), and wear resistance by 50–140% [43]. Under impact and rolling, the wear rate of Mn8 steel was 20% lower than that of Mn13 steel [44]. The authors attribute this effect to the greater sensitivity of Mn8 steel to strain hardening. During deformation, austenite can undergo either a martensitic phase transformation or twinning. Thus, two main mechanisms of strengthening of such steels are distinguished: transformation-induced plasticity (TRIP) [44,45] and twinning-induced plasticity (TWIP) [46]. These two strengthening mechanisms can achieve an optimal combination of mechanical parameters, exceptional abrasion resistance [47–50] and cost effectiveness [51]. It is known that the strengthening mechanism of austenitic steels depends on the stacking fault energy (SFE) [52]. At values below ~15 mJ/m$^2$, deformation induces ε-martensite (TRIP effect), whereas at higher SFE values twinning dominates (TWIP effect) [52]. In high-carbon MMA steels, SFE values typically range from 20 to 40 mJ/m$^2$ [52]. This level of stacking fault energy suppresses the direct $\gamma \rightarrow \alpha'$ martensitic transformation characteristic of the TRIP effect and activates the mechanical twinning mechanism (TWIP effect).

In the initial stages of impact and rolling abrasion, dislocation strengthening plays a major role. When the deformation reaches a certain extent, the deformation-induced martensitic transformation and twinning strengthening begin to play a leading role [44]. The strain-induced $\gamma \rightarrow \alpha'$ transformation occurs through the formation of an intermediated ε-martensitic phase, similarly to the stainless steels of 18Cr-8Ni type with metastable austenitic structure after high-rate and/or

 doi:10.20944/preprints202606.0435.v1



cryogenic straining [53–56]. Normally, the α′-martensite is formed at the increased strain extents on the twins' intersections or intersections of ε-martensitic lathes, and a maximum volume fraction of ε-martensite did not exceed ~10% [57]. Another situation is observed in high- or medium-manganese steels, which can contain up to 60% of ε-martensite [58–60].

Two different mechanisms of mechanical twinning are known to occur depending on the strain rate and stress magnitude (see Figure 1), i.e., a self-partial-multiplication (Figure 2a) or by the rebounding of partial dislocations on the grain boundary (Figure 2b). The first mechanism operates at a low strain rate and low stresses owing to Shockley dislocation reactions occurring within the stacking faults. Conversely, the partials' rebounding mechanism operates at a high strain rate and high stresses [61].

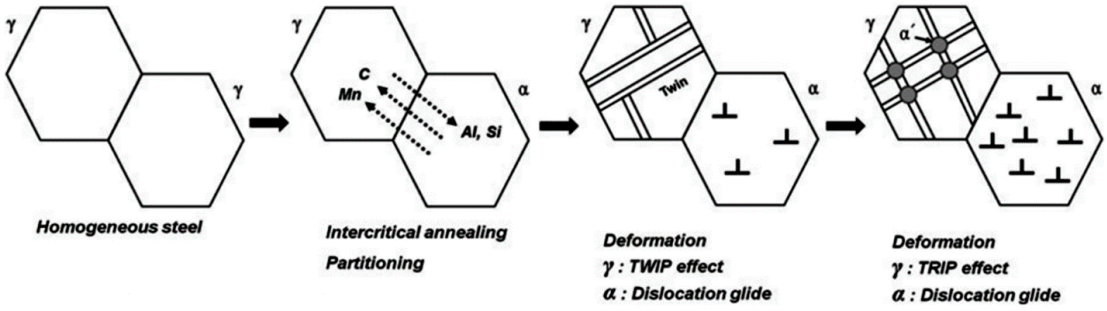


**Figure 1.** Mechanism of TWIP+TRIP in MMASs. Adapted from [60,61].

Lee's study [62] on Hadfield steels demonstrated the critical role of strain rate in determining the predominant strengthening mechanism. The authors found that at low loading rates, the structure evolves through the formation of ε-martensite. However, an increase in the deformation intensity suppresses the process of martensite formation, transferring the system to the mechanical twinning mode, which becomes a key factor in increasing plasticity [62]. The TRIP effect is a phenomenon in which the transformation of metastable austenite to martensite is induced at low stresses [44]. The mechanisms of strain hardening in MMA steels are determined by the TRIP and TWIP effects. The TRIP effect consists of a controlled transition of metastable austenite to martensite under the application of external loads [44]. Hardening in this case is caused by the barrier action of the matrix/martensite interphase boundaries, the redistribution of stresses in favour of the harder phase, and the limitation of transcrystalline slip due to the anisotropy of martensite precipitates [63]. In turn, the TWIP effect is realised through the continuous intersection of grains by deformation twins, which leads to structural fragmentation (dynamic grain refinement) and a consistent increase in dislocation density, providing a combination of high strength and ductility [64].

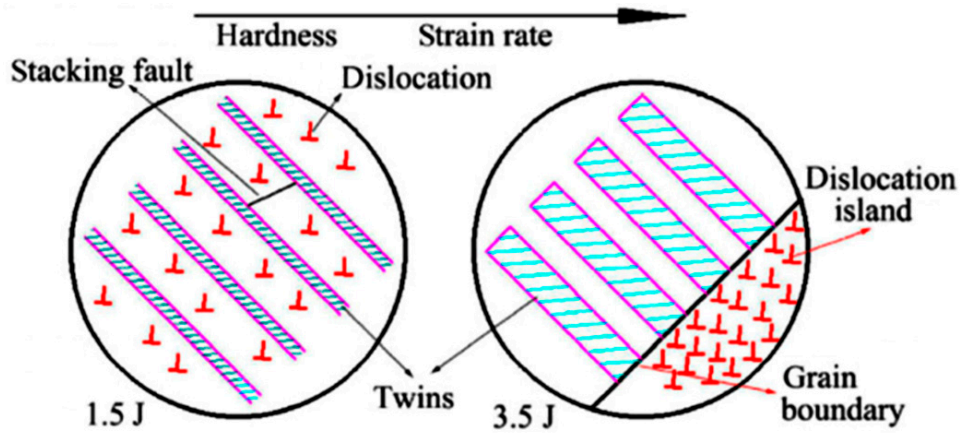

 doi:10.20944/preprints202606.0435.v1



**Figure 2.** Self-forming and impact-forming twins. Adapted from [49].

To evaluate the wear resistance of alloys, various abrasive wear test methods are used, such as pin-on-disc [65], ball-on-disc [51], ball-on-plate [66], and impact wear resistance test [46]. The interaction between the abrasive and the wear surface can occur through different mechanisms, such as micro-ploughing, micro-cutting, micro-fatigue, and microcracking [67], as well as cutting, wedging, and ploughing [68]. Chen et al. [49] used the same apparatus to determine the wear resistance at different impact energies from 0.5 to 6.0 J. The results showed that the best and worst wear resistance were observed at impact energies of 3.5 and 1.5 J, respectively. The degree of wear was related to changes in the amount of martensite, as well as the shape of dislocations and twins, at different impact energies. It was determined that the bulk morphology of martensite on the worn surface of medium-manganese steels does not change significantly under different impact conditions, while impact energy affects the morphology of dislocations and twins. Wang et al. [44] carried out impact and abrasive rolling wear tests using quartz sand particles between two steel rings. It was found that the impact and rolling wear rate of Mn8 alloy was 20% lower than that of Mn13 due to the better sensitivity of Mn8 to strain hardening.

Various technologies for mechanical hardening of metallic surfaces are used in practice, for example, shot peening [69,70], ultrasonic shot peening [71], surface mechanical attrition treatment [72], ultrasonic nanocrystalline surface modification (UNSM) [73], etc. Jia et al. [70] studied the effect of shot peening on the properties of medium manganese steel. The results of the study showed that after 30 min of shot peening processing, the hardness increases from ~286 HV in the initial state to ~477–480 HV in the treated state, forming a hardened layer up to 500 μm. Moreover, the main contribution to this strengthening is made by the formation of deformation twins with a thickness of 20–30 nm. Kim et al. [73] show that UNSM is an efficient method to overcome the current limitation of TWIP steel by enhancing the low YS during plastic deformation while preserving high strain hardening and large ductility.

High-frequency mechanical impact (HFMI) technology [74,75] (also known as ultrasonic impact treatment/peening (UIT/UIP) [76,77]) is an effective method for increasing the fatigue resistance of welded joints [74–76] and surface modification of metallic materials [76,77]. According to the literature, numerous attempts have been made to establish the effectiveness of ultrasonic methods of surface modification for improving the mechanical and microstructural properties of austenitic manganese steels. Recent research by Zhao et al. [71] demonstrates that UR treatment induces significant work hardening and grain refinement. The hardness increases from 286.77 HV to 632.28 HV, which changes the wear mode. The study by Meng et al. [78] focused on the effect of ultrasonic impact treatment (UIT) on the structural state and magnetic properties of austenitic high-manganese steel (Fe-17Mn-0.6C-1.5Al-0.3V). The results indicate that at room temperature, UIT initiates an intense TRIP effect, leading to a large-scale phase transformation of FCC austenite to BCC martensite ($\gamma \rightarrow \alpha'$). The proportion of the martensite phase on the surface increases from the initial 14.4% to 46%, accompanied by a sharp increase in microhardness from 310 HV to 580 HV. The main strengthening mechanism in this case is grain refinement and phase hardening [78]. It has been established that increasing the processing temperature to 300 °C (warm UIT) allows for the complete suppression of the transformation into martensite, while maintaining high hardness (approximately 515 HV) due to the formation of a stable nanocrystalline austenite structure and deformation-induced twinning (TWIP effect). Thus, varying the parameters of ultrasonic exposure allows for precise control of the phase composition and physical and mechanical properties of the surface layer, ensuring the required wear resistance without losing the non-magnetic properties of the material [78]. Trembach, Mordyuk et al. [79] investigated the effect of high-frequency mechanical forging (HFMF) on the microstructure, phase composition, and tribological characteristics of the deposited layer of high-manganese steel. The HFMI process variables were intensity, static load, and exposure duration. It was found that the increase in hardness (from HV0.2 = 2.78 GPa to $HV_{0.2}$ = 6–7.69 GPa) after HFMI treatment is associated with twinning, grain refinement, and increased lattice microstrain caused by an increase in dislocation density, the formation of ε martensite, and a small amount of $\alpha'$ martensite. It was

 doi:10.20944/preprints202606.0435.v1



established that HFMI process parameters have a significant impact on wear. The wear mechanism of the high-manganese steel studied varied from plastic deformation, leading to the formation of burrs in the initial state, to ploughing in the HFMI-hardened state. The most significant factor is the static load, which influences the surface modification of the high-manganese steel. The sample with a 150 N load, 10 μm amplitude, and 40 s duration demonstrated the highest wear resistance.

Surfacing processes are widely used both for strengthening surfaces and for restoring worn machine parts, providing a significant reduction in production costs due to the use of available structural steels as a base and extending the service life of components through local renovation of their geometry while simultaneously increasing wear resistance [80–86]. In modern engineering practice, a wide range of technologies are used to form functional coatings on parts made of various metals and alloys [86–93]. The most economical, accessible, and simple methods are arc surfacing [93]. Among the main methods of arc surfacing are shielded metal arc welding [94,95], gas tungsten arc welding [96,97], gas metal arc welding (GMAW) [98–100], submerged arc welding (SAW) [101,102], manual metal arc welding [103,104], and flux-cored arc welding (FCAW) [105–109]. In recent decades, special attention in the industry has been paid to the self-shielded flux-cored wire welding (FCAW-S) method, which is characterised by high productivity, technological flexibility, and the ability to produce deposited metal with specified operational properties [110–114]. An important issue is improving the quality of the deposited metal and the productivity of the surfacing process [110,114,115]. This problem is solved by introducing an exothermic additive into the filler of the flux-cored wire [116,117]. Numerous studies indicate an increase in the productivity of the process when introducing an exothermic additive into the filler of the flux-cored wire [115,117–121]. In [122], the influence of flux-cored wire surfacing (FCAW-S) modes with an exothermic additive of the $MnO_2$-Al system on the structural-phase state and mechanical properties of the deposited metal was investigated. It was found that the introduction of an exothermic mixture promotes grain refinement and modification of non-metallic inclusions (reduction in size and total quantity), which leads to an increase in the hardness and wear resistance of the coating. This is also confirmed by the earlier studies of Trembach et al. [122–124].

The aim of this work is to study the microstructure and mechanical properties of a surfacing made of high-carbon austenitic medium manganese steel alloyed with boron and titanium before and after modification using high-frequency mechanical impact treatment, as well as their effect on abrasive wear resistance.

## 2. Materials and Methods

### *2.1. Filler Material*

The experimental self-shielded flux-cored wire (FCAW-S) had a diameter of 4.0 mm and was specifically designed for the study. The core filler gave comprehensive gas and slag protection and provided controlled alloying and deoxidation of the weld pool. The wire's gas-and-slag-forming system belonged to the fluorite–rutile–carbonate type. A key feature was adding an exothermic component based on the MnO–Al thermite system. The detailed chemical composition of the core filler appears in Table 1. The oxidiser-to-reductant ratio matched stoichiometric proportions. Wire fabrication used a low-carbon steel strip (Grade St 24, DIN 1614.1) as the sheath material. The strip arrived annealed, with a width of 20 mm and a thickness of 0.5 mm. Core components were distributed within the formed U-shaped sheath, which was then closed and drawn in multiple stages. Each stage used calibrated dies to gradually reduce the diameter to the target of 4.0 mm. Coefficients of wire filling for the wires were 0.26.

 doi:10.20944/preprints202606.0435.v1



**Table 1.** Composition of core filler FCAW-SE, wt.%.

| The Name of the Component | Content of the Components in Core Filler of FCAW-S, [wt.%] | The Name of the Component | Content of the Components in Core Filler of FCAW-S, [wt.%] |
|---|---|---|---|
| Fluorspar GOST4421-73 | 11 | Ferrosilicon FS-75 GOST 1415-78 | 1 |
| Rutilovy concentrate GOST 22938-78 | 6 | Titanium powder PTM TU 14-22-57-92 | 2 |
| Calcium carbonate GOST8252-79 | 3 | Oxide of manganese powder-like GOST 4470-79 | 21.2 |
| Zirconium dioxide GOST 21907-76 | 2 | Aluminum powder PA1 GOST 6058-73 | 8.8 |
| Graphite is silver | 6 | Boron carbide ($B_4C$) powder | 3.2 |
| Metal Chrome X99 GOST 5905-79 | 6.5 | Iron powder PZhR-1 GOST 9849–86 | 13.8 |
| Ferromanganese FMN-88A GOST 4755-91 | 15.5 | | |

*2.2. Deposition Technology*

The deposition of the boron/titanium modified 140Mn6Cr3TiB steel was performed on S 235 J2G2 (St3ps) carbon steel substrates, compliant with the EN 10025-2 standard. The dimensions of the base metal plates were 200 × 100 × 15 mm. The cladding process was implemented using an A-874 automatic welding system (Paton Electric Welding Institute, Kyiv, Ukraine). The apparatus was integrated with a power source characterised by a constant-voltage (*CV*) output. The main deposition process parameters, i.e., wire feed speed (*WFS*), arc voltage (*Uset*), contact tip-to-work distance (*CTWD*) and travel speed (*TS*), were chosen based on the earlier performed studies and listed in Table 2.

 doi:10.20944/preprints202606.0435.v1



**Table 2.** Hardfacing parameters.

| Parameter | Recommended Range/Value |
|---|---|
| Wire diameter | 4.0 mm |
| Current (A) | 240 A |
| Arc voltage (V) | 22 V |
| Travel speed (m/h) | 20 m/h |
| Polarity / Current type | DC+, constant voltage |
| Position | Flat (downhand) |
| Preheating ($T_p$), [°C] | No |

After finishing the deposition process, specimens were cooled in still air to simulate industrial practice. The samples for microstructural examination, hardness profiling and wear testing were subsequently extracted from the overlays of the 140Mn6Cr3TiB steel according to the testing plan.

*2.3. High-Frequency Mechanical Impact Treatment*

To modify the near-surface microstructure of the 140Mn6Cr3TiB deposit, the HFMI treatment was used. Its principle [125,126] and the applied equipment [77,79,127] were described earlier. The used HFMI regimes provide various specific energies accumulated in the modified surface (Table 3). An ultrasonic generator (0.6 kW, $f_{US}$ = 21 kHz) supplied an acoustic setup with a piezoceramic transducer, a buster, and a step-like ultrasonic horn. Multiple high-frequency (~1 kHz) impacts of a needle-like Steel 52100 pin on the modified surface caused severe plastic deformation and microstructural changes in the near-surface layers of the treated specimen [128].

**Table 3.** Main parameters of HFMI treatment of the 140Mn6Cr3TiB deposit sample surface.

| Sample Marking | Apparatus Frequency (kHz) | Pin Impact Frequency (kHz) | Pin Material | Pin Diameter (mm) | Load (N) | Amplitude (μm) | HFMI Time (s) | Specific Accumulated Energy (kW/cm²) |
|---|---|---|---|---|---|---|---|---|
| 0 | - | - | - | - | 0 | 0 | 0 | 0 |
| 1 | | | | | 150.0 | 20 | 20 | 9.2 |
| 2 | 21.6 | 1±0.1 | Steel 52100 | 6 | 50.0 | 30 | 40 | 17.6 |
| 3 | | | | | 100.0 | 10 | 60 | 20.9 |

*2.4. Microstructure and Phase Analysis*

The surface morphology, microstructure, phase state and chemical compositions were analysed by scanning electron microscopy using a ZEISS EVO 40XVP microscope with an INCA energy dispersive X-ray spectroscopic (EDS) micro-analyser and a TESCAN Mira 3 LMU microscope equipped with an EDS micro-analyser OXFORD X-MAX 80 mm².

The microstructure and phase composition of the studied specimens were analysed by X-ray diffraction (XRD) analysis using a DRON-3 XRD apparatus with a Cu $K_\alpha$ source ($\lambda$ = 0.15406 nm) operated at a 'Θ–2Θ' focusing, step length of 0.04° and the residence time of 4 s. The crystallite size $D$, and lattice micro-strains η were based on the measured broadening ($B$), i.e., a full width at a half maximum (FWHM), and assessed physical broadening $\beta = (B^2 - b^2)^{1/2}$ ($B$ is FWHM and $b$ is instrumental broadening) of the (111), (200), (220), and (311) reflections using the Wiliamson-Hall approach and Debye-Scherrer equation [129]:

$$\beta = (K\lambda / D\cos\theta) + \eta \, \mathrm{tg}\theta, \quad (1)$$

where $K$ is the constant ($K$ = 0.9), $\lambda$ is the X-ray wavelength, and θ is the diffraction angle. The dislocation densities (ϱ) were estimated based on the XRD evaluated crystallite size ($D$), the lattice micro-strains (η), and Burgers vector for iron $b_B$ = 0.258 nm using the following formula [129,130]:

$$\varrho = 2\sqrt{3}\,\eta / (Db_B). \quad (2)$$

 doi:10.20944/preprints202606.0435.v1



To discriminate between the γ-, ε- and α`-phases, a deconvolution of the (111) maximums was performed using Origin Pro software. Comparing the intensity of (111) γ, (002) ε, and (110) α` sub-peaks obtained after deconvolution, a content of α`-phase was estimated, and a concentration of ε-phase $M_\varepsilon$ was also evaluated using the following formula [131]:

$$M_\varepsilon = \frac{100\%}{1+0.27\cdot\left(I_{111\gamma}/I_{002\varepsilon}\right)} \quad (3)$$

*2.5. Hardness and Wear Assessment Techniques*

The mechanical properties of the as-deposited specimens of the 140Mn6Cr3TiB steel were investigated by instrumented indentation with the Berkovich indenter using a multifunctional indentation tester "Micron-Gamma" at a load of 20 g and a loading rate of 2 g/s [132,133].

The same tester was also used to compare the tribological behaviour of the as-deposited and HFMI-treated specimens by evaluating their responses to the scratch tests. These tests were performed under the same controlled conditions using a conical diamond indenter with a tip radius of 50 μm, applying a constant predefined load. At the test beginning, the indenter was loaded to 500 mN over the first second, and then a 320 μm-long scratch track was formed on the specimen surface under this maximum constant load, and then the indenter was unloaded at 500 mN/s to finalise the test. Residual scratch depth was measured to numerically evaluate surface-layer wear. To eliminate initial surface roughness, a scratch-test procedure was performed in four steps: a pre-scan at low load for initial profile recording (320 μm), scratching under constant maximum load (320 μm), a post-scan to measure the formed scratch profile (320 μm), and finally subtracting the recorded scratch profile from the initial to determine the true scratch depth. Such a procedure for scratch characterisation enables a comparative assessment of tribological material properties across different surface roughness and surface slope (trend) [79,134]. The presented values of the scratch track depth were statistically averaged by three tracks situated as a 120° rosette, and they can be considered as a proxy for data related to the wear resistance of the studied surface.

Additionally, the micro-tribological tests were carried out in the reciprocating sliding mode using the ''Micron-gamma'' multifunctional tester equipped with a conical diamond indenter with a tip radius of 100 μm at a load of 500 mN. For this purpose, an additional reciprocating mechanism was installed on the movable stage of the indentation tester [135]. This test consisted of 170 cycles of reciprocating sliding at a constant normal load (0.49 N) on the indenter with simultaneous registration of the friction force. To measure the volume of the worn material, the wear tracks were analysed by the optical profilometer ''Micron-alpha'' [136,137].

Hertzian contact shear stress was assessed for the sphere d = 200 mkm to flat plate contact, and shear stress $\tau_{contact}$ in the specimen surface layer of ~10 μm thick was obtained to be ~1.7 GPa (with maximum value
$\tau_{max}$ = 2.17 GPa at a depth of ~3 μm).

## 3. Results

*3.1. Studies of the as-Deposited 140Mn6Cr3TiB Metal Hardfacing*

3.1.1. Microstructure and Phase Composition

The chemical composition of the deposited metal was evaluated using a Spectrolab LAVFC01A optical emission spectrometer (SPECTRO Analytical Instruments GmbH, Kleve, Germany) and listed in Table 4.

**Table 4.** The chemical composition of the deposited 140Mn6Cr3TiB metal (wt%).

| Element | C | Mn | Cr | Si | Ti | B | Al | N | P | S | Fe |
|---|---|---|---|---|---|---|---|---|---|---|---|
| Content (wt%) | 1.41 | 6.16 | 3.25 | 0.74 | 0.18 | 0.27 | 0.3 | 0.046 | 0.058 | 0.023 | Bal. |

 doi:10.20944/preprints202606.0435.v1



3.1.2. Theoretical Simulation and Analysis of Phase Stability

Based on the chemical composition of the deposited metal, a phase equilibrium diagram was modelled using JMatPro® API v7.0 software (Figure 3). This diagram serves as a tool for identifying critical temperatures and analysing the dynamics of phase transformations during heating or cooling.

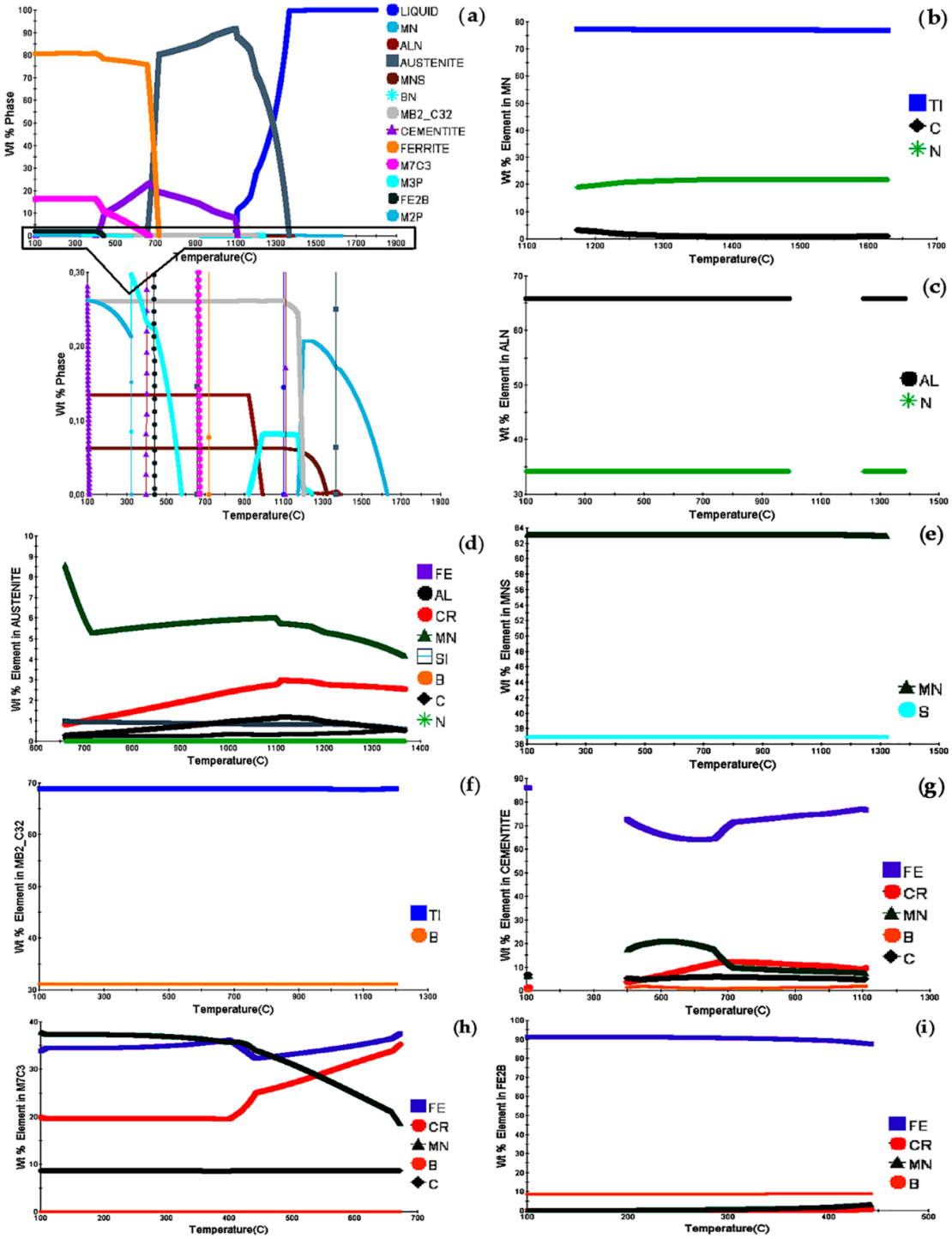


**Figure 3.** Calculation and prediction of phase type (**a**) and change in phase composition: (**b**) MN; (**c**) AlN; (**d**) Austenite; (**e**) MNS; (**f**) $MB_2\_C_{32}$; (**g**) Cementite; (**h**) $M_7C_3$; (**i**) $FE_2B$.

 doi:10.20944/preprints202606.0435.v1



An important feature of this alloy is the presence of refractory phases. Upon cooling of the molten weld pool at 1628.78 °C, precipitation of solid particles of titanium nitride TiN (Figure 4b) becomes thermodynamically possible. These particles contain approximately ~77 wt.% Ti over virtually the entire temperature range (Figure 4b). Upon further cooling to 1385.68 °C, precipitation of aluminium nitrides occurs (Figure 4c). Thus, the first phases to precipitate from the liquid solid solution are titanium and aluminium nitrides. These phases are dispersed and serve as modifiers that reduce the austenite grain size. Thermodynamic modelling of the solidification process of high-manganese steel 140Mn6Cr3TiB shows that the precipitation of primary γ austenite from the melt occurs at a liquidus temperature of approximately 1368.07 °C and is complete at a solidus temperature of 1100.22 °C. At 1321.07 °C, MnS sulphide inclusions precipitate from the alloy. At 1109.96 °C, the cementite phase precipitates from the supersaturated austenite solid solution. The fraction of cementite increases to ~16 vol.%. According to Figure 4e, in addition to iron (Fe), cementite contains significant amounts of manganese (up to 20–23 wt.%) and chromium (approximately 14 wt.%). This confirms the formation of alloyed cementite of the $(Fe,Mn,Cr)_3C$ type. Chromium and manganese exhibit significant interdendritic segregation, which facilitates the precipitation of complex secondary carbides ($M_7C_3$) along grain boundaries. Upon cooling below 672.63 °C, chromium carbides $M_7C_3$ with an fcc lattice precipitate from the solid solution. Analysis of Figure 4h shows that, due to the low chromium content, these carbides are rich in manganese and iron (the Cr content increases from 15% to 25% upon cooling) and manganese (~35–40%). $M_7C_3$ is formed from cementite, as can be seen from Figure 4a. Further cooling of the alloy leads to the transformation of austenite into ferrite (at 700.21 °C). With slow cooling below 1109.96 °C, the formation of titanium borides from previously formed TiN will be thermodynamically stable. At a temperature of 442.68, the low-temperature $Fe_2B$ phase is formed in the solution. Its mass fraction will be ~2 vol.%.

To initiate the transformation, high degrees of overcooling and prolonged holding at the appropriate temperatures are required. However, welding conditions are characterised by a nonequilibrium state due to the high cooling rate [138]. To analyse the matrix composition, it is advisable to use the built-in Welding Cycle calculation module. Figure 5 shows the continuous cooling transformation (CCT) diagram of the 140G6Kh3TV alloy under study, as well as the phase diagram under welding conditions with heating at a rate of 1000 °C/sec and cooling at a rate of CR = 67 °C/sec. Analysis of the CCT diagram (Figure 5a) showed that for a given chemical composition, the matrix will consist of an austenitic phase. This is also confirmed by modelling the phase composition for the given welding cycle conditions (Figure 5b). However, high welding deformations and stresses [123] will lead to the formation of martensite.

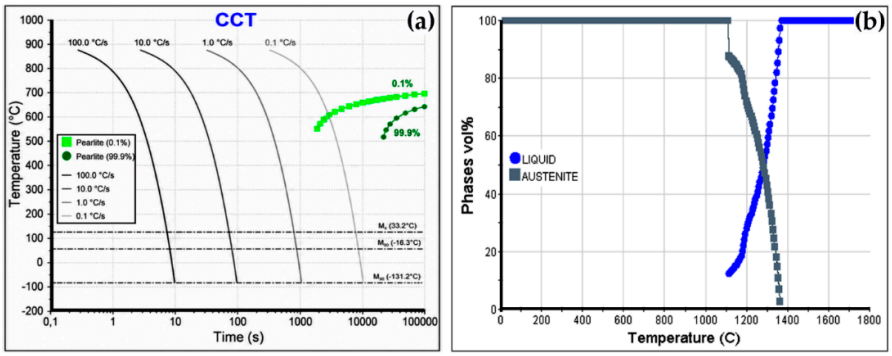


**Figure 4.** (a) Continuously cooling transformation (CCT) diagram and (b) phase composition during welding cycle (Rate of heating RH = 1000 °C/s, cooling rate CR = 45 °C) for the 140Mn6Cr3TiB deposited metal.

Preprints.org (www.preprints.org) | NOT PEER-REVIEWED | Posted: 8 June 2026 doi:10.20944/preprints202606.0435.v1



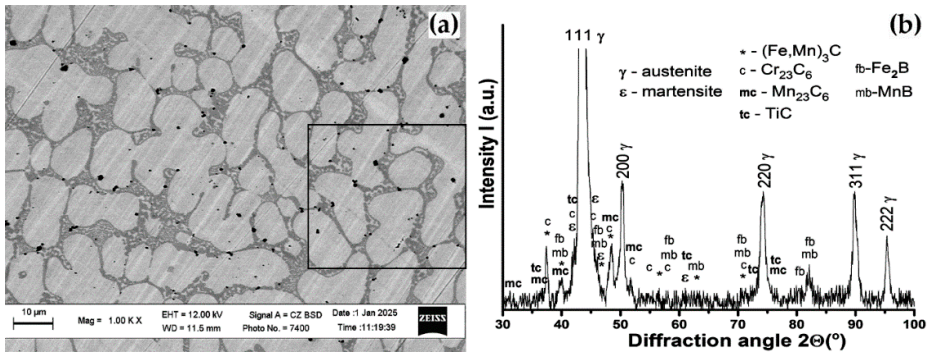


**Figure 5.** The SEM images of the microstructures x1000 (a) and XRD pattern (b) of deposited metal in 3 layers hardfacing by FCAW–SE-140Mn6Cr3TiB.

### 3.1.3. Microstructure and Phase Composition of as-Deposited Hardfacing

Figure 5a shows SEM observation of the microstructure of the as-deposited high-carbon austenitic middle-manganese steel 140Mn6Cr3TiB layer. The microstructure consists of irregularly shaped grains subdivided by interlayers with micro-heterogeneous eutectic-type morphology of various thicknesses. The XRD pattern of the deposit surface shown in Figure 5b confirms that it comprises the main austenitic matrix phase with face-centred cubic (FCC) lattice, intrinsic ε-phase with hexagonal close-packed (HCP) lattice, and numerous second phases, including carbides of various compositions as well as the iron and manganese borides. More detailed information regarding the chemical compositions of several constituents (Table 5) was obtained from the rectangular area marked in Figure 5a and shown at a higher magnification in Figure 6a together with the EDS spectra of the analysed microstructure constituents (Figure 6b,c,d).

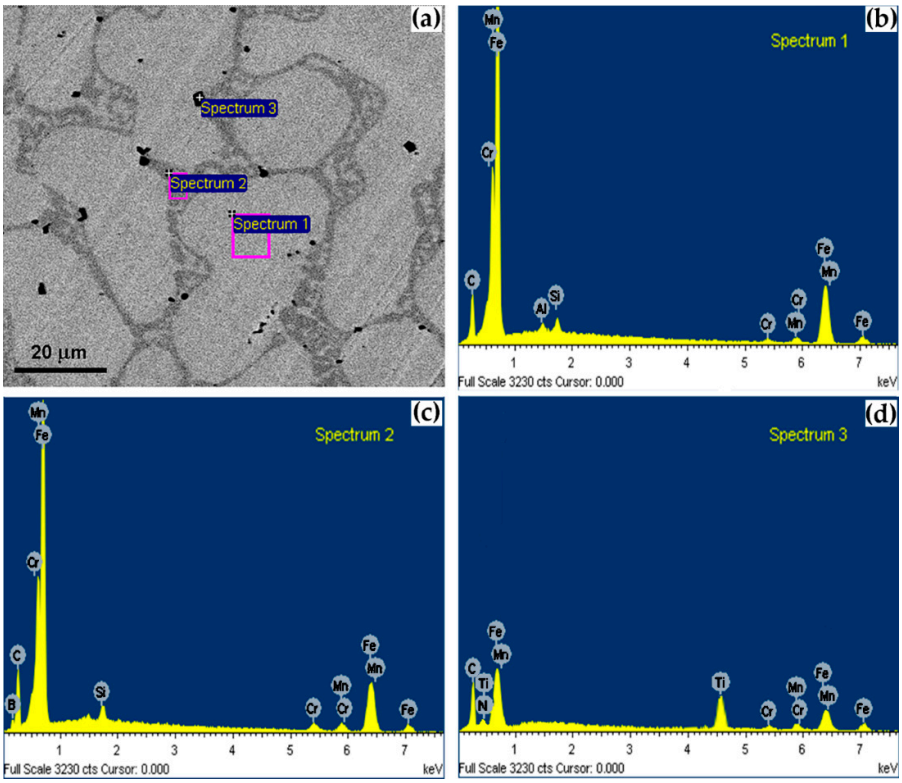


**Figure 6.** A higher magnification SEM image (a) of the microstructure of the area of 140Mn6Cr3TiB deposited metal marked in Figure 5a and EDS spectra (b, c, d) of the different phases indicated in (a).

 doi:10.20944/preprints202606.0435.v1



**Table 5.** Chemical compositions of constituent phases on PP-Np-90G13N4 deposited metal according to Figure 6a (mass.%/at.%).

| Analysed Area/Point | % | Alloying Elements, % | | | | | | | | | Phase |
|---|---|---|---|---|---|---|---|---|---|---|---|
| | | C | Mn | Fe | Cr | Ti | Al | B | N | Si | |
| Spectrum 1 | Weight | 4.72 | 4.88 | 85.53 | 1.86 | - | 0.38 | 0.74 | - | 0.62 | matrix (γ-austenite + ε-martensite) |
| | Atomic | 20.27 | 3.95 | 68.1 | 1.59 | - | 0.63 | 3.06 | - | 0.97 | |
| Spectrum 2 | Weight | 7.06 | 7.54 | 76.68 | 4.57 | 0.23 | 0.13 | 2.75 | - | 0.47 | Boride–Carbide interlayer $Fe_2B$, MnB, (Fe,Mn,Cr)C |
| | Atomic | 23.5 | 5.49 | 54.88 | 3.52 | 0.19 | 0.2 | 10.15 | - | 0.67 | |
| Spectrum 3 | Weight | 2.77 | 15.72 | 10.52 | 8.23 | 53.89 | - | - | 9.11 | 2.61 | TiN, $Me_xC_y$ |
| | Atomic | 9.11 | 11.31 | 7.45 | 6.26 | 44.51 | - | - | 17.69 | 3.67 | |

The EDS analysis of the deposited 140Mn6Cr3TiB high-carbon MMAS revealed the formation of a heterogeneous multiphase structure consisting of an Fe–Mn–Cr austenitic matrix, intergranular carbide-austenite eutectic containing borides and Ti-rich secondary precipitates. The microstructure of the studied MMAS in the as-cast state is characterised by a pronounced dendritic morphology, as shown in Figure 5a and Figure 6a. The EDS analysis allowed for the evaluation the chemical partitioning between the structural constituents (Table 5). The primary dendritic matrix (spectrum 1), representing the light-contrast phase in the BSE mode, consists of a solid solution of alloying elements in iron. The elemental analysis shows that these regions are primarily composed of iron (approx. 85.53 wt.%) with a moderate content of manganese (4.88 wt.%) and chromium (1.86 wt.%). This phase corresponds to the austenitic matrix (Figure 6a) containing ε-phase (Figure 5b).

In contrast, the interdendritic regions (Spectrum 2) exhibit a darker grey contrast, indicating an enrichment of lighter elements and solutes with lower partition coefficients. Moreover, it appears not to be a homogeneous solid solution but a micro-heterogeneous mixture of austenite and secondary phases. The EDS data for this area reveals a significant segregation of carbon (up to 7.06 wt.% / 23.5 at.%), boron (up to 2.75 wt.% / 10.15 at.%) as well as relatively high contents of manganese (5.49 at.%), chromium (4.57 at.%), and some titanium (0.19 at.%), which indicates that this area contains many carbides and borides (see XRD spectrum in Figure 5b). This chemical signature suggests the formation of a eutectic-like structure consisting of alloyed carbides, iron and manganese borides, and manganese-enriched austenite in the interdendritic interlayers. Alongside the matrix, secondary carbide phases may include Fe–Mn carbides of the $(Fe,Mn)_3C$ type or $(Fe,Mn)_2C$, as well as the chromium-containing ones. These carbides exhibited markedly elevated carbon contents (up to 23.5 at.%) and locally higher Mn concentrations, indicating preferential segregation of Mn during carbide formation. More accurate identification of crystalline lattice and content of these carbides ($M_7C_3$ vs $M_{23}C_6$) would require additional investigations using electron back-scattering diffraction or selective area electron diffraction in a transmission electron microscope. The variation in Mn and Cr concentrations between the analysed regions suggests dendritic micro-segregation during rapid solidification, typical for self-shielded flux-cored arc welding.

In contrast, the localised Ti-enriched particles containing up to ~44 at.% of Ti were identified as titanium carbide or carbonitride phases, most probably TiC and TiN. These precipitates formed due to the high chemical affinity of titanium to carbon during nonequilibrium crystallisation. They acted as hard reinforcing phases within the austenitic matrix. Enrichment of these particles with Mn (~11 at.%) suggests that some manganese carbides can also be formed. These features had direct consequences for tribological performance: the hard Mn-rich carbides would contribute to improved resistance against abrasive and adhesive wear by providing load-bearing, work-hardening sites. Additionally, the observed phase composition is consistent with the microstructural features commonly reported for high-manganese hardfacing alloys, where the combination of metastable austenite and dispersed carbide particles provides enhanced wear resistance and strain-hardening

 doi:10.20944/preprints202606.0435.v1



capability under abrasive loading. Furthermore, distinct dark inclusions with sharp geometric shapes were observed throughout the microstructure. These particles are characterised by a high concentration of titanium (44.51 at.%), nitrogen (17.69 at.%), and carbon (9.11 at.%). Observation of some contents of other elements (Mn, Fe, Cr) in the analysed small-size phase constituent relates to the contribution of the neighbour reflecting matrix to the registered EDS spectrum. The presence of TiN suggests that titanium acts as a grain refiner and nitrogen scavenger during solidification.

3.1.4. Mechanical Properties of the Deposited Metal

Wear is the result of a complex reaction of the tribosystem, and it is largely determined by the mechanical properties of the tribosystem's components. The behaviour of complex tribosystems that undergo shock abrasive, hydro-abrasive, or cavitation wear is determined by a set of properties. Many researchers are looking for the correlation of individual mechanical properties with abrasive wear resistance, such as: Vickers hardness (HV), ultimate tensile strength (UTS) and yield strength (YS), strain hardening exponent ($n$), uniform elongation (UE), etc. [139–141]. One of the modern methods of determining mechanical properties is instrumental indentation. This method allows for evaluating a number of indicators from the registered loading-unloading curves. These indicators, i.e., indentation hardness $H_{IT}$ and contact elastic modulus $E_{IT}$, are useful for the prediction of the wear properties through the assessment of ductility index $H_{IT}/E_{IT}$, plastic deformation index $H_{IT}^3/E_{IT}^2$, and the index of tolerance to abrasion damage $1/(E_{IT}^2 \cdot H_{IT})$ collected in Table 6. The load-unload curves and indents are shown in Figure 7.

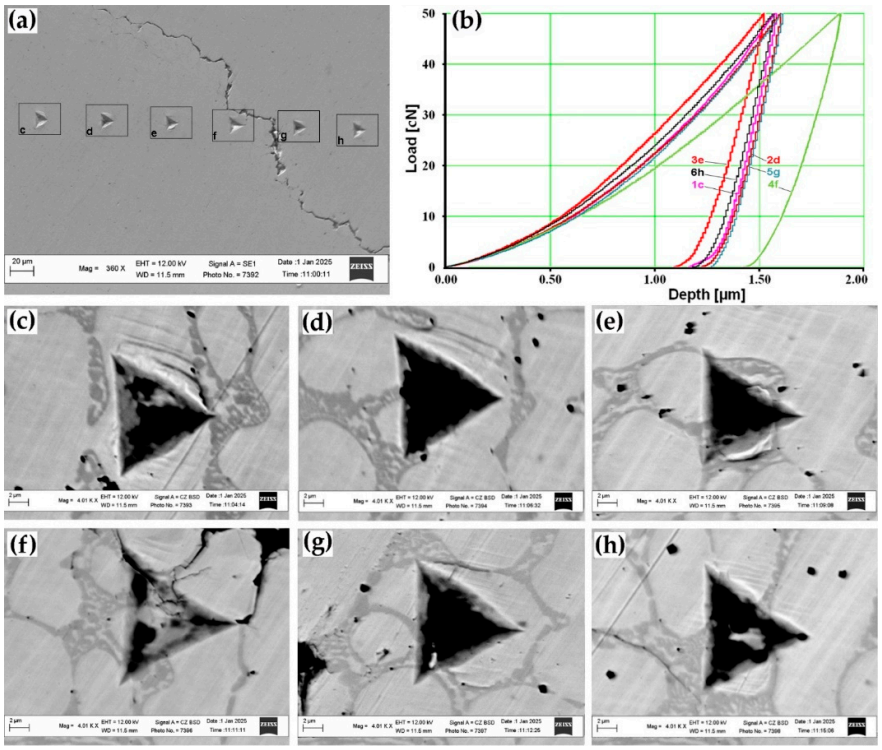


**Figure 7.** (a) SEM observations of nanoindents on the specimen surface layer deposited using the powder wire FCAW–SE-140Mn6Cr3TiB, (b) the registered loading-unloading "load P – depth" graphs, and SEM observations of nanoindents at a magnification x2000: (c) Indent 1; (d) Indent 2; (e) Indent 3; (f) Indent 4; (j) Indent 5; (h) Indent 6.

Within the framework of fracture mechanics, fundamental metrics such as fracture toughness and the critical energy release rate play a pivotal role in assessing material failure [142]. The stress fields and localised displacements in the vicinity of a pre-existing crack tip are conventionally

 doi:10.20944/preprints202606.0435.v1



described by the stress intensity factor. Concurrently, the energy release rate G defines the variation of potential energy across the evolving crack surfaces [143]. Consequently, G exhibits a direct mathematical correlation with the stress intensity factor, serving as a highly effective, complementary criterion for evaluating structural toughness. Therefore, the fracture toughness was assessed using Irving's expression [144]:

$$K_C = \sqrt{G \cdot E_{IT}} \quad (4)$$

where G is the strain energy release rate, $E$ is the contact elastic modulus.

Table 6 collects the mechanical properties of various areas of the 140Mn6Cr3TB alloy deposit sample, and Table 7 contains the evaluated parameters that allow for examining the tolerance of the studied deposit to abrasion damage.

In this case, on SEM images, the place of traces of the indents can show deposits of the matrix phase (white phase) pressed into the material, which indicates their high plasticity. The morphology of the deformation zone around the Berkovich indenter impression (Figure 8c,d) is characterised by the formation of distinct slip and twinning bands oriented along the close-packed {111} planes, which is typical for austenitic steels. According to Efstathiou and Sehitoglu's results [145], these structures represent mesoscopic packets of deformation twins. This is confirmed by the interband spacing measured in this study, ranging from 0.4 to 2.5 μm (Figure 8c,d). The reduction in the interband spacing ($L$) as one approaches the indenter faces indicates an exponential increase in the density of twin boundaries, which act as insurmountable barriers to dislocations (the dynamic Hall-Petch effect) [145]. This heterogeneous nature of deformation and the intersection of primary and secondary twin systems observed at the indentation periphery result in an abnormally high strain hardening coefficient of the material, which is a key factor in resisting micro-ploughing and adhesive wear under intense tribological contact conditions. The magnified indentation location of indenter 4 shows the formation of a crack propagating along the interdendritic eutectic. This is consistent with general concepts of fracture in austenitic medium- and high-manganese alloys.

**Table 6.** Mechanical properties of the initial specimen of the 140Mn6Cr3TiB deposited metal.

| Indent | Phase | Indentation | | Macro-Mechanic Properties | | Strain Energy |
|---|---|---|---|---|---|---|
| | | Hardness $H_{IT}$, GPa | Modulus $E_{IT}$, GPa | Microhardness $HV_{0,05}$ (±2...3%) | Elastic Modulus $E_S$, GPa (±5...10%) | Release Rate, $G$ [GPa] |
| Indent 1 | Austenitic matrix | 7.87 | 218.2 | 741 | 268 | 2.08 |
| Indent 2 | Austenitic matrix | 7.66 | 222.4 | 722 | 274 | 2.03 |
| Indent 3 | Boride–Carbide interlayer | 8.45 | 245.4 | 796 | 252 | 2.24 |
| Indent 4 | Cracked Boride–Carbide interlayer | 5.53 | 180.1 | 521 | 178 | 1.47 |
| Indent 5 | Boride–Carbide interlayer | 8.6 | 240.1 | 716 | 245 | 2.01 |
| Indent 6 | Austenitic matrix+ interlayer | 8 | 240.8 | 754 | 246 | 2.11 |

**Table 7.** Parameters of the initial specimen of the 140Mn6Cr3TiB deposited metal affecting abrasion resistance.

| Indent | Phase | Fracture Toughness $K_C$ (MPa·m$^{1/2}$) | Ductility Index $H_{IT}/E_{IT}$ | Plastic Deformation Index $H_{IT}^3/E_{IT}^2$ [МПа] | Index of Tolerance to Abrasion Damage $1/(E_{IT}^2 \cdot H_{IT}) \cdot 10^{-6}$ [МПа$^{-3}$] |
|---|---|---|---|---|---|
| Indent 1 | Austenitic matrix | 23.17 | 0.030 | 7.312 | 62.53 |

 doi:10.20944/preprints202606.0435.v1



| | | | | | |
|---|---|---|---|---|---|
| Indent 2 | Austenitic matrix | 23.08 | 0.029 | 6.528 | 64.95 |
| Indent 3 | Boride–Carbide interlayer | 23.45 | 0.034 | 10.019 | 57.07 |
| Indent 5 | Boride–Carbide interlayer | 21.97 | 0.036 | 11.033 | 56.31 |
| Indent 6 | Austenitic matrix+ interlayer | 22.54 | 0.033 | 8.830 | 64.89 |

Analysis of the obtained data shows that the deposited metal has relatively uniform properties. The presence of a carbide phase in the eutectic leads to a slight increase in microhardness and a decrease in the elastic modulus. The mechanical properties of the matrix (in Figure 8c,d, corresponding to the light phase) will be described by the indentations labelled Indent 1 and Indent 2. Whereas the eutectic would correspond to the indentations with the indices Indent 3 and Indent 5, since, according to Figure 8e, g, they fall within the grey phase. The indentation with the index Indent 6, according to Figure 8h, falls on the boundary between the light and grey phases. The matrix hardness is $H_{IT}$ = 7.66–7.87 GPa, and the instrumental modulus $E_{IT}$ = 218.2–222.4 GPa. Such high values of mechanical properties can be associated with strong deformation during nanoindentation [146–148]. The indentation region is expected to consist of two phases: original austenite and transformed ε-martensite [147,148]. Hardening is indicated by the formation of bands around the puncture sites, which are particularly pronounced for punctures hitting the matrix (Figure 8c,d) and less pronounced for the eutectic (Figure 8e,h). Such high nanoindentation hardness values ($H_{IT}$ = 7.65 ± 0.25 GPa) for a deformed sample were also obtained by Weidner et al. [149], and He et al. [147], which obtained nanoindentation hardness values of $H_{IT}$ = 7.7 GPa. While for the austenitic matrix, an average value of about 6.15 ± 0.25 GPa was determined [149]. Therefore, an increased dislocation density (regular dislocations and/or stacking faults) in the austenite is contributing to the higher value of indentation hardness.

The eutectic in the interdendritic region has a higher hardness ($H_{IT}$ = 8.45–8.6 GPa) and a lower modulus of elasticity ($E_{IT}$ = 240.1–245.4 GPa) compared to the matrix. The structural complexity of the investigated steel prevents direct measurement of discrete nanoprecipitates via nanoindentation. Therefore, the results reflect a combined hardness, accounting for both the primary matrix and the secondary nanoprecipitate phases ($M_{23}C_7$ carbides and $Fe_2B$ boride). These microhardness values can be explained by the presence of hard carbides $(Mn,Cr,Fe)_{23}C_7$, as well as the strengthening of the austenitic matrix via the TRIP mechanism during indentation with a Berkovich indenter.

Thus, the experimental alloy under consideration has a high average microhardness while retaining its hardenability. This makes it promising for abrasive wear under moderate impact loads.

The increase in $H/E$ directly correlates with the increase in the material's load-bearing capacity, allowing the structure to effectively resist external loads without exceeding the elastic deformation limits [150]. This parameter, also defined as the plasticity index, serves as an indicator of energy dissipation during destructive processes [151,152]. Analysis of nanoindentation parameters showed that the eutectic phase is characterised by higher values of the plasticity index ($H/E \approx 0.034–0.036$ versus $H/E \approx 0.029–0.030$ for the matrix) and the plastic deformation resistance index ($H^3/E^2$ = 11.033 MPa versus $H^3/E^2$ = 6.528–7.312 MPa for the matrix) compared to the matrix. Austenite and ε-martensite have lower hardness compared to carbides and borides, so they are more susceptible to plastic flow under load. On the contrary, the relatively low value of the plasticity index for the matrix indicates a higher capacity for macroplastic deformation before the onset of failure. When an abrasive impacts the matrix, the latter does not chip, but plastically deforms, absorbing the impact and scratch energy. Thus, the matrix will demonstrate greater resistance to abrasive wear compared to the eutectic. This is indicated by the higher value of the index of tolerance to abrasion damage ($1/(E^2H)$=(62.53–64.95)·$10^{-6}$ $MPa^{-3}$. for the matrix, versus $1/(E^2H)$ = (56.31–57.07)·$10^{-6}$ $MPa^{-3}$) for the interdendritic region.

 doi:10.20944/preprints202606.0435.v1



Based on the Hollomon equation ($\sigma = K\varepsilon^n$), the variation of the strain hardening exponent n as a function of the true strain, ε, is plotted in Figure 8. All graphs show a nonlinear relationship between lnσ and lnε, indicating two-stage strain hardening with different deformation mechanisms for the small-strain regime (initial plasticity) and the large-strain regime (extended plastic deformation). The first regime characterised the initial plastic deformation immediately after yielding, up to ε = 0.03. The second regime was recorded after line alignment. This change in mechanical behaviour is closely related to the evolution of the microstructure and the deformation mechanism of the material [153].

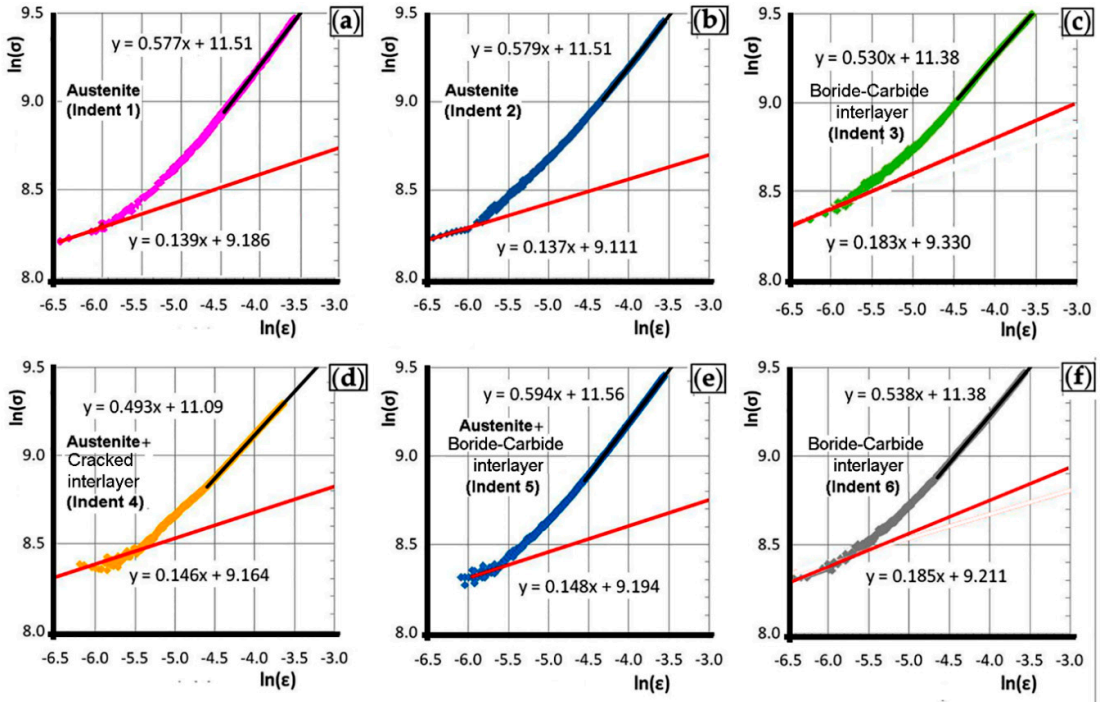


**Figure 8.** Logarithmic plots of representative flow stress versus representative plastic strain for six nanoindentation tests (Indents *I*1–*I*6). The strain hardening exponents were determined by linear regression in two ranges of plastic strain: ε ∈ [0.14–0.25] ($n_1$, small-strain regime) and ε ∈ [0.25–0.41] ($n_2$, large-strain regime). The fitted lines and corresponding $R^2$ values are shown on each subplot.

The strain-hardening exponents ($n$) derived from six nanoindentation points on the deposited 140Mn6Cr3TiB metal were summarised in Table 8.

**Table 8.** Strain hardening exponents ($n_1$ and $n_2$) of 140Mn6Cr3TiB deposited metal.

| Indent | Phase | Strain-Hardening Exponent | |
|---|---|---|---|
| | | *Small-Strain Regime* $n_1$ | *Large-Strain Regime* $n_2$ |
| Indent 1 | Austenitic matrix | 0.139 | 0.577 |
| Indent 2 | Austenitic matrix | 0.137 | 0.579 |
| Indent 3 | Boride–Carbide interlayer | 0.181 | 0.530 |
| Indent 5 | Austenitic matrix + Boride–Carbide interlayer | 0.148 | 0.594 |
| Indent 6 | Boride–Carbide interlayer | 0.185 | 0.538 |

Analysis of nanoindentation curves allowed us to determine the strain hardening coefficient for various structural components of 140Mn6Cr3TiB steel in two deformation modes: small-strain ($n_1$) and large-strain ($n_2$). For the matrix phase consisting of austenite and ε martensite, n1 values vary within the range of 0.137–0.148, indicating moderate hardening intensity at the initial stage of

 doi:10.20944/preprints202606.0435.v1



indentation. The transition to large deformations is characterized by a sharp jump in the $n_2$ coefficient to values of 0.577–0.579. Such a significant increase (more than 4 times) is explained by the development of strain hardening of austenite under the indenter (TRIP/TWIP effects) [154] and are in good agreement with previously obtained results of other researchers [154,155]. This is indicated by high hardness values and the presence of clear slip bands and twinning.

The eutectic phase (austenite with chromium carbides and iron borides) exhibits n1 values in the range of 0.183–0.185, which is comparable to or slightly higher than the matrix values. Under high deformation conditions, the $n_2$ coefficient reaches 0.530–0.594. Despite the high hardness of carbide and boride inclusions, the presence of an austenite component in the eutectic provides it with a high potential for strengthening with increasing load. The spread of values in this case may be due to the heterogeneity of the distribution and orientation of the hard particles relative to the indenter penetration axis.

### *3.2. HFMI-Induced Microstructure Changes*

Figure 9a shows the results of XRD analysis of the structure-phase state of the specimens' near-surface layers of the as-deposited and HFMI-treated 140Mn6Cr3TiB high-carbon MMAS. As seen, the XRD patterns of the HFMI-treated specimens contain new diffraction peaks appeared owing to the strain-induced $\gamma \rightarrow \varepsilon$ and $\gamma \rightarrow \varepsilon \rightarrow \alpha'$ martensitic transformations additionally to the high-intensity peaks of austenitic phase (FCC γ-Fe), borides ($Fe_2B$, MnB) and several carbide phases, i.e., manganese/chromium doped cementite $(Fe,Mn,Cr)_3C$, manganese and chromium carbides $Mn_{23}C_6$, $Cr_{23}C_6$, and probably titanium carbide TiC. Diffraction peaks of the austenite matrix phase appear to be broadened after HFMI, which is a result of dislocation density increase, crystallite refinement, and lattice microstrains' increase evaluated using Eqs (1,2) (see Table 9 for quantitative data). Similar peak broadening effect was observed by XRD analysis of the ultrasonically hardened stainless steel [156]. Figure 9b presents the enlarged fragments of the XRD patterns describing the HFMI-induced asymmetry and shift of the (111) and (200) peaks of the austenitic phase, which are known to be the result of the appearance of the random deformation faulting of the FCC lattice according to Eq (5) [131,157]. According to a classic work by Paterson [160], the appearance of the random deformation faults in the austenitic lattice results in the displacement of the diffuse components of diffraction maxima and/or shifts of their centroids. Moreover, the (111) and (200) peaks (as well as the other pairs of peaks) are normally shifted towards each other on the diffraction angle axis, and this shift first manifests itself by the uneven distribution of the maximum intensities, i.e., by the appearance of the peaks' asymmetries on the higher-angle and lower-angle sides of the (111) and (200) peaks, respectively (Figure 9b). This asymmetry is caused by summing the contributions from the various diffraction components, a sharp one reflected from the deeper sub-surface layers and a diffuse one formed owing to the reflection from the top surface layer. The quantitative data regarding the concentration of random stacking faults ($\alpha_\Sigma$) in γ-austenite were evaluated considering the mutual shift of Bragg angles of (200)γ and (111)γ reflexes, their Bragg angle θ positions using the formula (5) [131] and presented in Table 7.

$$\Delta(2\theta_{200} - 2\theta_{111}) = \frac{45\sqrt{3}\,\alpha_\Sigma\,(2tg\theta_{200} - tg\theta_{111})}{2\pi^2}. \quad (5)$$

 doi:10.20944/preprints202606.0435.v1



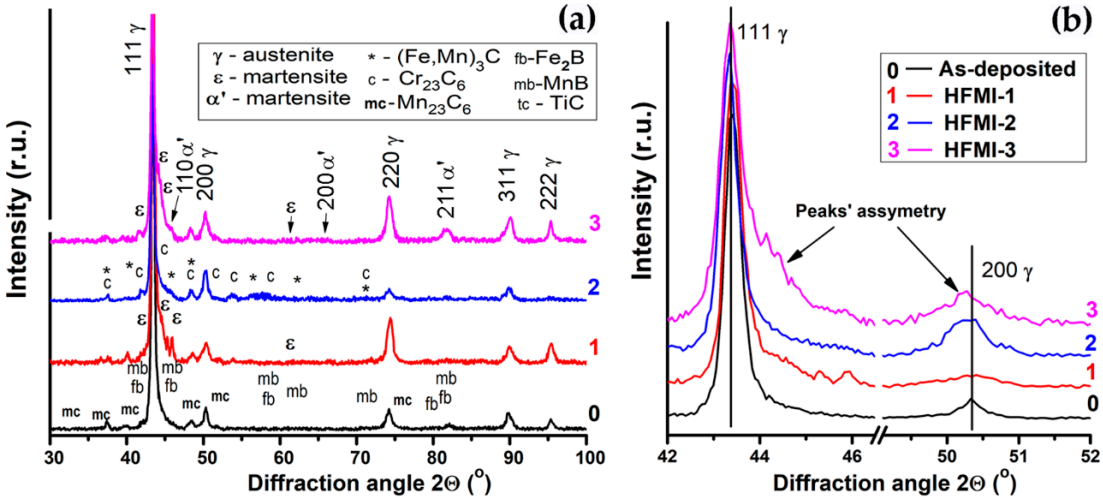


**Figure 9.** XRD patterns (a) and fragments (b) of the initial as-deposited (0) and HFMI-processed specimens: HFMI-1 (1), HFMI-2 (2), and HFMI-3 (3).

The increased volume fraction of the stacking faults in the FCC lattice is known to result in the formation of ε-martensite with HCP lattice, which diffraction peaks have angle positions in the vicinity of the (111) peak of FCC γ-austenite. To analyse the phase composition in more detail, a closer consideration and deconvolution of the (111) γ peak of the initial and HFMI-treated specimens was performed (Figure 10). As evaluated, the (111) peak of the as -deposited 140Mn6Cr3TiB high-carbon MMAS contains subpeaks related to the matrix γ-phase and ε-phase reflecting the presence of stacking faults in the γ-matrix (Figure 10a). The HFMI processes caried-out using various regimes resulted in broadening and pronounced asymmetry of the XRD peaks of γ-phase and clearer manifestation of carbide and borides phases (Figure 10b–d). Moreover, a comparison of the deconvoluted (111) γ peak of the HFMI-treated specimens allowed observing additional sub-peak related to the α`-phase with base-centred tetragonal (BCT) lattice (Figure 10b–d), which is known to form at the expense of the ε-phase (ε-platelets' intersections) at the intersection of twins. The volume fraction of the ε-martensite was assessed using Eq. (3), and peaks' intensity comparison was used to estimate the content of α`-martensite. These data were also listed in Table 9. The volume fractions of both martensitic phases were grown with the increase in the impact energy accumulated during the HFMI process. However, the content of α`-martensite remains relatively low, changing from ~2–3.5% to ~6% for HFMI-3 treatment. Conversely, the content of ε-martensite achieves up to 66%, which is in line with the literature data reporting a similar volume fraction (50–60%) of ε-martensite formed in the high-manganese steels [158] or middle-manganese steels after cold rolling to the strain extent of 15–20% [159].

**Table 9.** Microstructural parameters, microhardness and hardening depths of the middle-manganese steel.

| Sample Marking | Accumulated Impact Energy (kW/cm²) | Hardening Depth (LOM) (μm) | Surface Microhardness HV (200 g) (GPa) | Crystallite Size D (nm) XRD | Lattice Microstrains η (%) | Dislocation Density ϱ (cm⁻²) | Concentration of Random Stacking Faults in γ-Austenite | Volume Fraction (%) | | Worn Depth (μm) |
|---|---|---|---|---|---|---|---|---|---|---|
| | | | | | | | | ε | α′ | |
| 0 | 0 | 0 | 5.17 | 1260 | 0.02 | $2.1 \cdot 10^{11}$ | 0.0560 | 50.3 | 3.4 | 0.518 |
| 1 | 9.2 | 11.9 | 7.58 | 54 | 0.1 | $2.2 \cdot 10^{13}$ | 0.0561 | 52.9 | 2.1 | 0.427 |
| 2 | 17.6 | 21.4 | 7.66 | 32 | 0.12 | $5.1 \cdot 10^{13}$ | 0.0563 | 65.4 | 4.2 | 0.41 |
| 3 | 20.9 | 27.8 | 7.77 | 31 | 0.118 | $5.09 \cdot 10^{13}$ | 0.0566 | 66.0 | 5.7 | 0.375 |

 doi:10.20944/preprints202606.0435.v1



In worth to be noticed that HFMI straining not only results in the martensitic transformations (analysis showed that $M_\varepsilon$ assessed using Eq.(3) for the initial state was 50.3% and it increases to ~53%, 65%, and 66% in the HFMI-1, HFMI-2, and HFMI-3 specimens, respectively (Table 9)), but it also significantly increases the dislocation density at least in austenite (see broadened austenitic peaks in Figure 9a and Table 9). At the same time, the martensite phases also seem to continuously strengthen due to an increase in dislocation density with the HFMI process applied. The dislocation-mediated deformation mechanisms are known to be one of the most frequently operated in the deformed metallic materials. First of all, this concerns the so-called wavy-slip materials with medium or high stacking fault energies [160] (including the $\alpha$`-martensite considered here). Besides, low stacking fault energy materials, such as stainless steels [56,161] or high- and medium-manganese steels [53,60] are deformed due to dislocation activity, which operates simultaneously or at the expense of the twinning [162]. At the same time, the warm rolling process is more conducive to the formation of high-density dislocation structures in BCC and FCC phases of medium-manganese steel than hot rolling due to the temperature-facilitated relaxation of the formed defects. It was reported by Zhang et al. that a fraction of small and medium angle grain boundaries is higher in the warm-rolled specimens [162]. Moreover, the increase of pre-strain was reported to significantly rise the dislocation density within the martensite phase, leading to additional strength increase. The experimental results obtained after HFMI correlate well with the literature data. Indeed, the hardness increase in the HFMI-modified near-surface layer was registered both by the indentation tests (Table 7) and Vickers hardness measurements (Table 9). The XRD-based assessment reveals the increase in the dislocation density on two orders of magnitude, which essentially affects material hardness additionally to grains/crystallites refinement assessed to be of a nano-scale (31–54 nm) and to the formation of two martensitic phases (Table 9). The nano-scale grains are known to contribute to the material strength according to the well-known Hall-Petch relation extensively discussed in the literature [56,77,79,163,164] and to the wear resistance [165–167]. Additional factor affecting the wear resistance is the heterogeneous microstructure of alloyed austenite grains subdivided by a harder carbides/borides containing interlayers formed after deposition (Figure 5a, Figure 6a) and highly-dislocated and partially transformed microstructure of the deformed austenite containing numerous ε- and $\alpha$`-martensite platelets/grains after HFMI (Table 9).

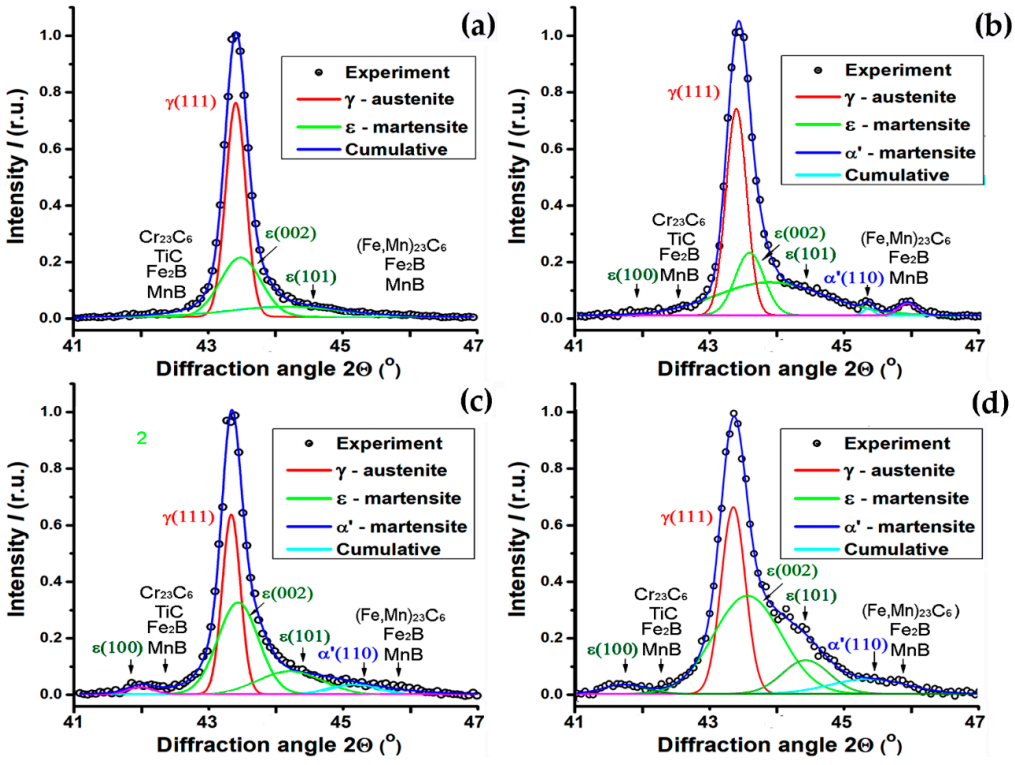

 doi:10.20944/preprints202606.0435.v1



**Figure 10.** Fragments of the XRD patterns with deconvoluted (111) peaks for the initial (a) and HFMI processed specimens: HFMI-1 (a), HFMI-2 (b), and HFMI-3 (c).

### *3.3. Effects of HFMI on Wear Behaviour*

#### 3.3.1. Scratch Test Results

Wear behaviour of the as-deposited and HFMI-treated 140Mn6Cr3TiB high-carbon MMAS was studied using the scratch tests, which have become a convenient and powerful tool for evaluating tribological properties of materials [168], coating-substrate adhesion [169], and substructural changes in thin surface layers [**170**]. Figure 11a–c shows the recorded scratch tracks profiles formed after scratch testing of the HFMI-treated specimens in comparison with the profile observed in the initial surface. The SEM images of the scratch track views are also shown for the initial as-deposited (Figure 11d), HFMI-1-treated (Figure 11e), HFMI-2-treated (Figure 11f), and HFMI-3-treated (Figure 11g) surfaces. As seen, all the HFMI-treated surfaces better withstood the applied loading as the scratch track depths (as shown in Figure 11a–c and listed in Table 9 as worn depths) and the scratch track widths (indicated in Figure 11d–g) were lower than those registered for the initial specimen.

Figure 12 presents the retrieved, statistically analysed data on the evolution of average track depth, which correlates with the tribological properties of the surface layers formed after deposition and following HFMI treatment. As seen, the track depths on the studied HFMI-treated surfaces decrease with increasing HFMI intensity. This correlates with the HFMI-induced surface hardening related to the formation of the refined grains of austenitic and martensitic phases (Table 7, Table 9) and indicates the increase in the wear resistance of the HFMI-treated surfaces.

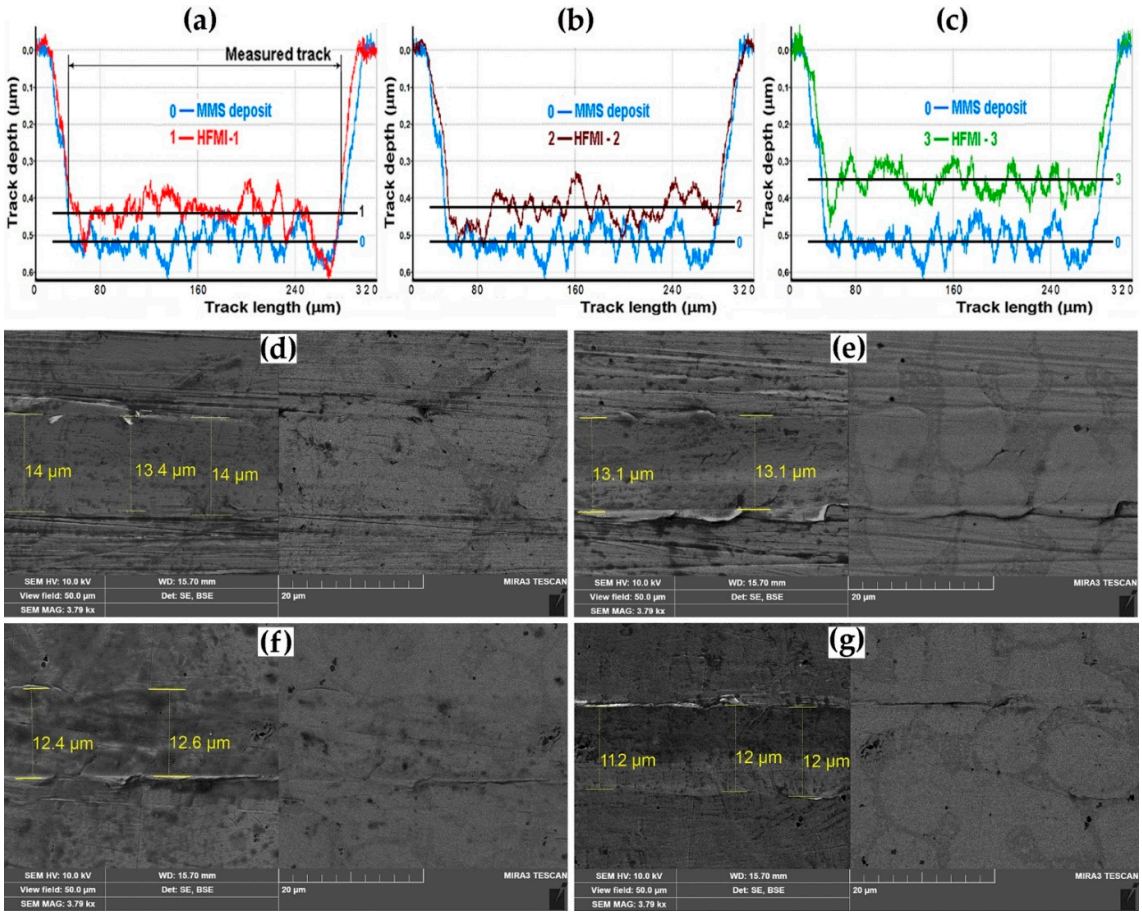

 doi:10.20944/preprints202606.0435.v1



**Figure 11.** The registered profiles (a–c) and SEM observations (d–g) of the scratch tracks formed on the initial (a–d), HFMI-1 (a, e), HFMI-2 (b, f), and HFMI-3 (c, g) treated surfaces.

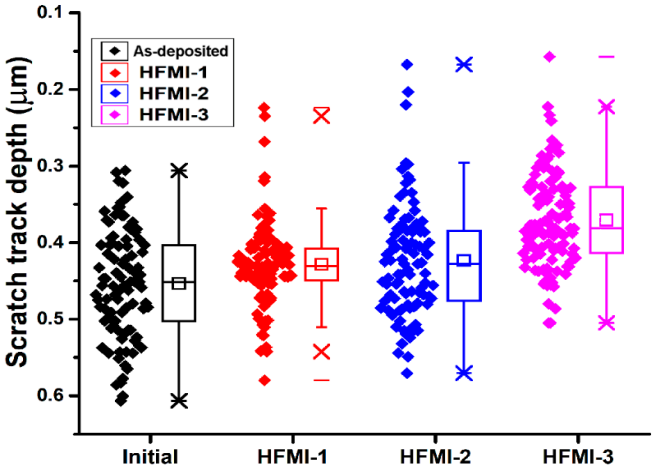


**Figure 12.** Statistically evaluated scratch track depths formed on the initial middle-manganese steel deposit before and after HFMI treatment of various regimes: HFMI-1, HFMI-2, and HFMI-3.

The same trend was also observed in the micro-tribological tests, which better represent real service conditions and possible abrasive wear. These tests were carried out in the reciprocating sliding mode. Figure 13 shows the sliding tracks obtained for the as-deposited and HFMI-3 treated specimens. The SEM images of the grooves formed after the sliding tests supplemented with their 2D profiles (Figure 13a,c) are accompanied with the light interferential 3D profiles (Figure 13b,d). As seen, the HFMI-3-treatment is confirmed to result in approximately a half decrease in the sliding track and about four times decrease in the wear volume from 15.2 μm$^3$ down to 3.9 μm$^3$ (indicated in Figure 13b,d). Again, the harder the surface is, the higher the wear resistance of this surface is. This observation is in line with the well-known inverse proportionality of hardness and wear usually described by the Archard-Rabinovitz relation connecting wear $W$ with applied pressure $P$, the material's hardness $H$, and wear coefficient $k$ accounting for the material's ductility $K$ [165,166,171]:

$$W = K\,P\,/H \qquad (6)$$

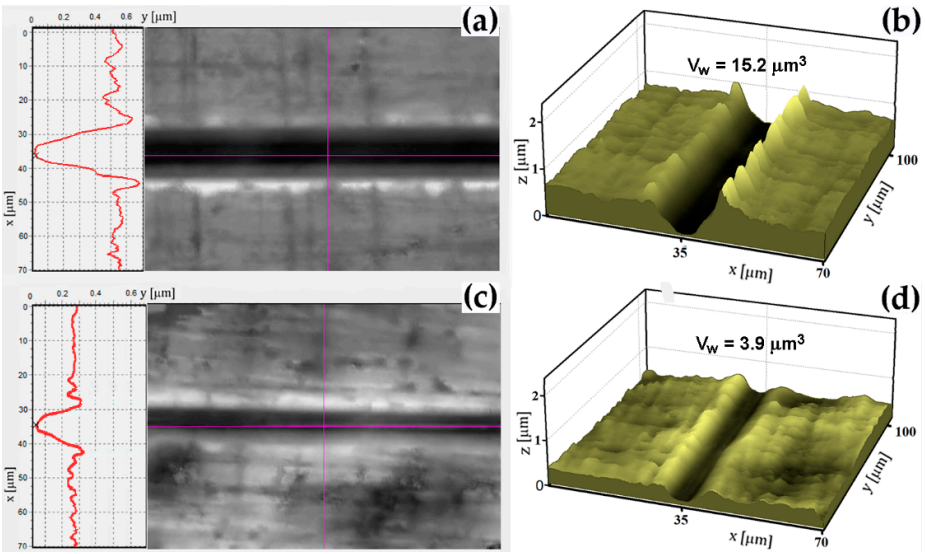

 doi:10.20944/preprints202606.0435.v1



**Figure 13.** Statistically evaluated scratch track depths formed on the initial middle-manganese steel deposit before and after HFMI treatment of various regimes: HFMI-1, HFMI-2, and HFMI-3.

The above-mentioned inverse proportionality of hardness and wear is also visible in Figure 14 collecting the dependencies of the surface hardness and scratch track depth on the accumulated impact energy at the HFMI treatment. The increase in the Vickers hardness observed after HFMI treatment of the deposited metal, which is assessed to be about 31%, correlates well to the ~37% decrease in the registered scratch track depth.

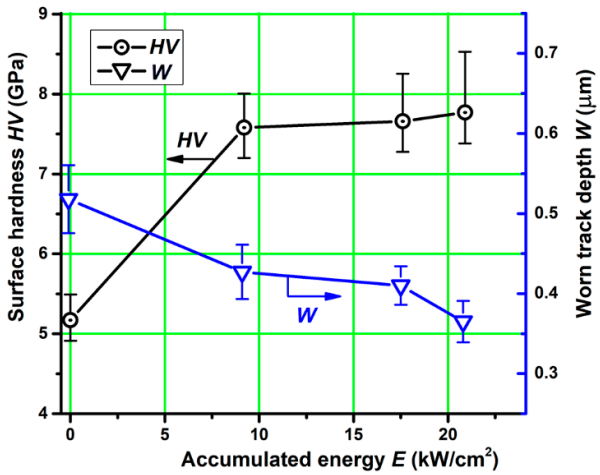


**Figure 14.** Dependencies of surface hardness of the 140Mn6Cr3TiB MMAS deposit, and worn track depth on the accumulated impact energy applied at the HFMI treatment.

## 4. Discussion

Following our previous studies [79,130], we analyse the operating wear mechanisms using an approach suggested by Kato et al. [68,172]. In this approach, the wear mechanisms are considered in a graph connecting the severity of the contact between the tested surface and spherical counterbody, on the one hand, and properties of the tested material. A parameter $D_P$, which characterises the degree of penetration of the spherical counterbody during a single test cycle, is thought to describe the severity of the contact between the tested surface and spherical counterbody. On the other hand, a $f$ parameter is considered to be equal to the ratio of the shear stress at the contact surface $\tau_{contact}$ assessed for the Hertzian contact to the bulk shear stress $\tau_{0.2}$ of the wearing material. The areas in the graph with the ordinate ($D_P$) and abscissa ($f$) axes, are related to the operating wear mechanisms. Fortunately, the test conditions, i.e., the contact area, the counterbody radius $R$, the load $P$, and properties of the tested material (microhardness HV and bulk shear stress $\tau_{0.2}$ related to the yield stress as $\sigma_{0.2}/\sqrt{3}$), are also taken into account by $D_P$ by the following relation [68,130,172]:

$$D_p = R\sqrt{\frac{HV}{2P}} - \sqrt{\left[\frac{HV}{2P}\right]R^2 - 1} \qquad (7)$$

The calculated values of the $D_P$ parameter estimated according to Eq. (7) for the tested 140Fe6MnTiB steel specimens in the initial and HFMI-treated states were shown in the '$D$ vs $f$' graph (Figure 15). The theoretical boundaries dividing the areas of various operating wear mechanisms according to Kato et al. [68,172], i.e., cutting, wedge (pile-ups forming), and ploughing, are indicated by the solid lines in Figure 15. Thus, the graph shown in Figure 15 contains the theoretical (solid lines [68,172]) and experimental data (open squares) for 1045 steel from Ref. [68,172]. Additionally, several sets of experimental data are also shown for various steels: the open triangles [130] stand for laser hardened and HFMI-treated 1045 steel, the open and solid circles for the shot-blasted Fe23Mn [46] and HFMI-hardened Fe12Mn3Ni [79] steels, respectively.

 doi:10.20944/preprints202606.0435.v1



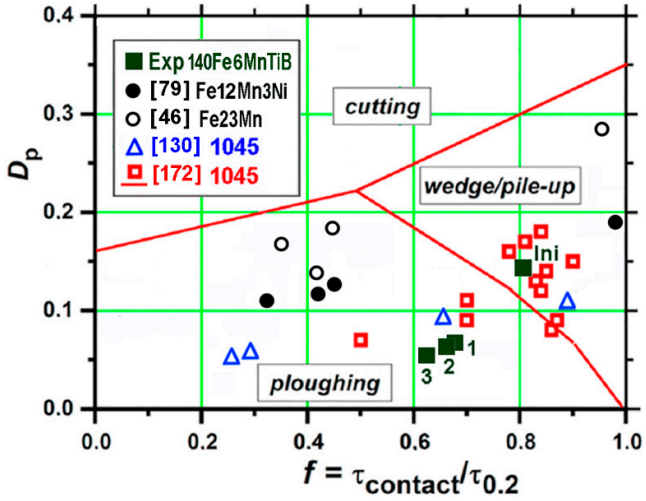


**Figure 15.** Dependence of the $D_P$ parameter on the $f$ parameter describing the ratio of the shear stress at the contact surface to the bulk shear stress wearing material. Lines/open squares and open triangles are respectively related to 1045 steel studied in references [172] and [130], open and solid circles stand for shot blasted Fe23Mn alloy [46] and HFMI-treated Fe12Mn3Ni steel [79].

The evaluated data positioned in Figure 15 indicate that the initial specimen of 140Fe6MnTiB steel was situated in the 'wedge/pile-up' area that is in line with the other Fe-Mn steels regardless the manganese content (Fe23Mn [46] and Fe12Mn3Ni [79]). Conversely, the ploughing mechanism of wear became predominant for the HFMI treated samples instead of the plasticity dominated wear observed for the initial specimen owing to the HFMI-induced stain hardening and plasticity exhaustion. However, as compared to the HFMI-hardened 90Fe12Mn3Ni steel [80], the border with 'wedge/pile-up' area is much closer. This correlated well to the experimentally observed pile-ups formed along the tracks after scratch (Figure 11) and wear (Figure 13) of the 140Fe6MnTiB steel. Additionally, the values of $D_P$ for the HFMI-processed specimens of 140Fe6MnTiB steel were three times smaller than the value assessed for the initial deposit. This indicates much higher resistance of the HFMI-hardened surface of the 140Fe6MnTiB steel deposit to the penetration of the spherical counterbody. For the HFMI-treated 140Fe6MnTiB steel deposits, the morphologies of the worn surfaces contained some ploughings (Figure 11c–d), which quantity and depth however are much lower than those observed for 90Fe12Mn3Ni steel [79] owing to the heterogeneous microstructure, namely the harder boride/carbide eutectic interlayers and hardened austenite matrix with fine Ti(C,N) particles (Figure 5, Figure 6, Figure 11, Table 5). Similar beneficial influence of manganese carbides [36] and titanium carbonitrides [70] was reported for MMAS. In a high carbon Fe-Mn-C austenitic alloy, was prone to form a strong C-Mn bond network at subgrain boundaries, which could constrain the movement of solute atoms and strongly hinder the initiation of slip systems and the movement of dislocations. In addition, C-Mn atomic pairs could also strongly interact with the strain field of dislocations, further increasing dislocation density by pinning effects [36]. At the same time, severe shot-peening regime was reported to become less beneficial and even slightly adverse due to overgeneration of dislocation around Ti(C,N) particles, which may lead to critical decrease in the impact toughness and deterioration in the wear resistance [70,173]. Additionally, the extreme hardening of the top surface layer of the laser-remelted high-manganese steel by ultrasonic rolling supplemented with the plasticity decrease was also concluded to become deteriorative for fatigue crack initiation [71]. Due to overloading, the formation of numerous multisystem twins beneath the top hardened layer may prevent the extension of the deformed layer deeper into the material, and may thus facilitate the exfoliation of the overhardened layer during wear test.

 doi:10.20944/preprints202606.0435.v1



## 5. Conclusions

The microstructural peculiarities and properties of the of titanium and boron-alloyed high-carbon medium-manganese 140Mn6Cr3TiB steel deposit before and after high-frequency mechanical impact (HFMI) treatment were studied in this paper. The obtained results allow us to draw the following conclusions:

1. The micromechanical investigation of the 140Mn6Cr3TiB steel deposit through nanoindentation revealed a distinct correlation between the phase composition and the deformation behaviour. The austenitic-martensitic matrix exhibits high ductility and a superior index of tolerance to abrasion damage (up to 64.95), while the eutectic constituent, composed of chromium and manganese carbides and iron and manganese borides, provides the necessary structural rigidity with a significantly higher plastic deformation resistance (up to 11.033 MPa). The heterogeneous nature of the steel creates a "shield-and-buffer" effect, where the hard eutectic framework resists penetration and tough matrix prevents brittle failure.
2. A critical finding is the dual-regime strain-hardening behaviour observed in both structural constituents. In the large-strain regime ($n_2$), the strain-hardening exponent increases substantially, reaching values of 0.577–0.579 for the matrix and up to 0.594 for the eutectic phase. This pronounced hardening capability, likely driven by dislocation density evolution and potential strain-induced phase transformations (TRIP/TWIP effects) in the metastable austenite, ensures that the material maintains its integrity and resistance to localised wear even under severe contact loading.
3. The synergistic interaction between the phases is further evidenced by the properties of the transition zones (Matrix + Eutectic), which follow the rule of mixtures while maintaining a high tolerance to abrasion damage (64.89). This indicates that the 140Mn6Cr3TiB steel deposit effectively combines the high hardness of boride-carbide phases with the high fracture toughness of the manganese-rich austenite. Such a mechanical profile makes this alloy highly suitable for applications involving intense abrasive-impact wear, where a balance between hardness and energy dissipation is paramount.
4. The HFMI treatment results in the formation of the strain-induced ε- and $\alpha'$-martensites (~66% and 3–6%, respectively), a significant grains/crystallites refinement (down to 31–54 nm), and dislocation density (~$2.2*10^{13}$–$5.1*10^{13}$ $cm^{-2}$), which support essential hardening from $HV_{0.2}$ = 5.17 GPato$HV_{0.2}$ ≈ 7.8 GPa.
5. The HFMI treatment regime (load = 100 N**,** amplitude = 10 μm, and HFMI time = 60 s) is found to be optimum. It leads to the enhancement in wear resistance of 140Mn6Cr3TiB steel hardfacing that manifests itself by the decrease of the wear volume by ~4 times from 15.2 $\mu m^3$ to 3.9 $\mu m^3$ and in the decrease in the scratch track depths by ~30% (from ~0.52 μm to ~0.37 μm) in comparison with the initial deposit.
6. The HFMI-hardening changed the wear mechanism of titanium and boron-alloyed high-carbon medium-manganese 140Mn6Cr3TiB steel deposit to the ploughing mechanism instead of the 'wedge/pile-ups' formation operated in the as-deposited hardfacing.

**Author Contributions:** Conceptualization, B.T. and B.M.; methodology, B.T. and B.M.; software, B.T., V.K., and V.Z.; validation, P.O., O.K., M.K., V.S., and O.G.; formal analysis, P.O., V.Z., V.S., Y.M, and O.K.; investigation, B.T., B.M., T.V, M.S., V.Z., and V.K.; resources, B.T. and M.K.; data curation, M.S., V.Z., T.V., O.K., V.K., Y.M, and O.G.; writing—original draft preparation, B.T. and B.M.; writing—review and editing, M.K., B.M., and V.S.; visualization, B.M., B.T., and V.Z.; supervision, B.M., B.T. and V.S.; project administration, B.T. and B.M.; funding acquisition, B.T., M.K., B.M., and V.Z. All authors have read and agreed to the published version of the manuscript.

**Funding:** This research received no external funding.

**Data Availability Statement:** The original contributions presented in this study are included in the article. Further inquiries can be directed to the corresponding authors.

 doi:10.20944/preprints202606.0435.v1



**Acknowledgments:** This work was supported by the Scientific Grant Agency of the Ministry of Education, Research, Development and Youth of the Slovak Republic and the Slovak Academy of Sciences (VEGA), project No. 1/0260/26: "Experimental research on the optimization of Q&P heat treatment parameters to increase the tribological resistance of advanced high-strength AHSS steels with medium Mn content." Studies are partially supported by National Academy of Sciences of Ukraine (State Reg. No. 0123U102368) and the National Research Foundation of Ukraine under the program "Advanced Science in Ukraine 2026-2028"(State Reg. No. 0126U003263).

**Conflicts of Interest:** The authors declare no conflicts of interest.

## Abbreviations

The following abbreviations are used in this manuscript:

| | |
|---|---|
| ASTM | American Society for Testing and Materials |
| FCAW | Flux-Cored Arc Welding |
| FCAW-S | Flux-Cored Arc Welding Surfacing |
| GMAW | Gas Metal Arc Welding |
| TRIP | Transformation-Induced Plasticity |
| TWIP | Twinning-Induced Plasticity |
| HFMI | High-Frequency Mechanical Impact |
| UIT/UIP | Ultrasonic Impact Treatment / Ultrasonic Impact Peening |
| UNSM | Ultrasonic Nanocrystalline Surface Modification |
| XRD | X-Ray Diffraction |
| FWHM | Full Widths at Half Maximum |
| SEM | Scanning Electron Microscopy |
| EDS | Energy Dispersive Spectroscopy |
| HV | Vickers Hardness |
| BCC | Base Centred Cubic |
| BCT | Base Centred Tetragonal |
| FCC | Face-Centred Cubic |
| HCP | Hexagonal Close-Packed |
| SFE | Stacking Fault Energy |
| CCT | Continuous Cooling Transformation |
| MMAS | Medium-Manganese Austenite Steel |

## References

1. Bulloch, J.H.; Henderson, J.L. Some Considerations of Wear and Hardfacing Materials. *Int. J. Pressure Vessels and Piping*, **1991**, *46*, 251–267.
2. Tandon, D.; Li, H.; Pan, Z.; Yu, D.; Pang, W. A Review on Hardfacing, Process Variables, Challenges, and Future Works. *Metals* **2023**, *13*, 1512. https://doi.org/10.3390/met13091512
3. Efremenko, V.G.; Chabak, Yu.G.; Shimizu, K.; Golinskyi, M.A.; Lekatou, A.G.; Petryshynets, I.; Efremenko, B.V.; Halfa, H.; Kusumoto, K.; Zurnadzhy, V.I. The Novel Hybrid Concept on Designing Advanced Multi-Component Cast Irons: Effect of Boron and Titanium (Thermodynamic modelling, microstructure and mechanical property evaluation). *Mater. Characterization* **2023**, *197*, 112691, https://doi.org/10.1016/j.matchar.2023.112691
4. Hlushkova, D.B.; Bagrov, V.A.; Saenko, V.A.; Volchuk, V.M.; Kalinin, A.V.; Kalinina, N.E. Study of Wear of the Bulding-up Zone of Martensite-Austenitic and Secondary Hardening Steels of the Cr-Mn-Ti System. *Problems Atomic Sci. Technol*. **2023**, *144*, 105–109. https://doi.org/10.46813/2023-144-105.
5. Teixeira, M.F.; Pacheco, J.T.; da Silva, L.J.; Rabelo, A.; Pereira, M.; Niño, C.E. Laser Cladding of Metco 1040® (Fe-V-Mn-C) on Hadfield Steel: Effect of Processing Parameters on Microstructure and Wear Resistance. *Opt. Laser Technol.* **2021**, *142*, 107219. https://doi.org/10.1016/j.optlastec.2021.107219

 doi:10.20944/preprints202606.0435.v1




6. Krawczyk, J.; Pawłowski, B. The Analysis of the Tribological Properties of the Armoured Face Conveyor Chain Race / badania własności tribologicznych płyty ślizgowej przenośnika zgrzebłowego. *Arch. Min. Sci.* **2013**, *58*, 1251–1262.
7. Okechukwu, C.; Dahunsi, O.A.; Oke, P.K.; Oladele, I.O.; Dauda, M. Development of Hardfaced Crusher Jaws using Ferro-Alloy Hardfacing Inserts and Low Carbon Steel Substrate. *J. Tribol.* **2018**, *18*, 20–39.
8. Krauze, K.; Mucha, K.; Wydro, T.; Pawlik, J.; Wróblewska-Pawlik, A. Mass and Volumetric Abrasive Wear Measurements of the Mining Conical Picks. *Sustainability* **2023**, *15*, 850. https://doi.org/10.3390/su15010850
9. Gülenç, B.; Kahraman, N. Wear Behaviour of Bulldozer Rollers Welded Using a Submerged Arc Welding Process. *Mater. Design*, **2003**, *24*(7), 537-542. https://doi.org/10.1016/S0261-3069(03)00082-7
10. Kostencki, P.; Stawicki, T.; Królicka, A. Wear of the Working Parts of Agricultural Tools in the Context of the Mass of Chemical Elements Introduced into Soil During its Cultivation. *Int. Soil and Water Conservation Research*, **2021**, *9*(2), 229-240. https://doi.org/10.1016/j.iswcr.2020.11.001
11. Kostencki, P.; Stawicki, T.; Krolicka, A.; Sędłak, P. Wear of Cultivator Coulters Reinforced with Cemented-Carbide Plates and Hardfacing. *Wear*, **2019**, *438*, 203063.
12. Lesyk, D.A.; Martinez, S.; Mordyuk, B.N.; Dzhemelinskyi, V.V.; Lamikiz, A.; Prokopenko, G.I.; Milman, Yu.V.; Grinkevych. K.E. Microstructure Related Enhancement in Wear Resistance of Tool Steel AISI D2 by Applying Laser Heat Treatment Followed by Ultrasonic Impact Treatment. *Surf. Coat. Technol.* **2017**, 328, 344–354. https://doi.org/10.1016/j.surfcoat.2017.08.045
13. Singh, J.; Chatha, S.S.; Sidhu, B.S. Abrasive Wear Characteristics and Microstructure of Fe-based Overlaid Ploughshares in Different Field Conditions. *Soil and Tillage Research*, **2021**, *205*, 104771. https://doi.org/10.1016/j.still.2020.104771
14. Liu, W.; Bell, A.; Wang, Z.; Zhang, Z.; Kovacevic, R. Evaluation of the Slurry Erosion Resistance of the Body Materials of Oil & Gas Drill Bits with a Modified Abrasive Waterjet. *Wear*, **2020**, *456*, 203364. https://doi.org/10.1016/j.wear.2020.203364
15. Hebib, M.; Choukrane, L.; Cheniti, B.; Faghi, L;, Kovalčíková, A.; Bouchafaa, H.; Maamache, B. Csanádi, T.; Hvizdoš, P. Recovery of Metal Matrix Composite Drilling Tools using a WC-Ni/Cr TIG-Hardfacing Technology. *Wear*, **2024**, *540*, 205273. https://doi.org/10.1016/j.wear.2024.205273
16. Myamlin, S.; Neduzha, L.; Urbutis, Ž. Research of Innovations of Diesel Locomotives and Bogies. *Procedia Eng.* **2016**, *134*, 470–475. https://doi.org/10.1016/j.proeng.2016.01.069
17. Oo, H.Z.; Muangjunburee, P. Hardfacing of Thermite Welded Rail by Flux-cored Arc Welding. *Wear* **2024**, *546*, 205314. https://doi.org/10.1016/j.wear.2024.205314
18. Bondarenko, I.; Lunys, O.; Neduzha, L.; Keršys, R. Dynamic Track Irregularities Modeling when Studying Rolling Stock Dynamics. In Proceedings of the 23rd Int. Sci. Conf. Transport Means, Palanga, Lithuania, 2–4 October 2019; pp. 1014–1019.
19. Bondarenko, I.; Lukoševičius, V.; Keršys, R.; Neduzha, L. Investigation of Dynamic Processes of Rolling Stock–Track Interaction: Experimental Realization. *Sustainability* **2023**, *15*, 5356. https://doi.org/10.3390/su15065356
20. Magalhães, K.M.M.; Brasil, R.M.L.R.F.; Wahrhaftig, A.M.; Siqueira, G.H.; Bondarenko, I.; Neduzha, L. Influence of Atmospheric Humidity on the Critical Buckling Load of Reinforced Concrete Columns. *Int. J. Struct. Stab. Dyn.* **2022**, *22*,2250011. https://doi.org/10.1142/S0219455422500110.
21. Tandon, D.; Li, H.; Pan, Z.; Yu, D.; Pang, W. A Review on Hardfacing, Process Variables, Challenges, and Future Works. *Metals* **2023**, *13*, 1512. https://doi.org/10.3390/met13091512
22. Sukhova, O.V. Effect of Ti, Al, Si on the Structure and Mechanical Properties of Boron-Rich Fe–B–C Alloys. *East. Eur. J. Phys.* **2021**, *2021*, 115–121. https://doi.org/10.26565/2312-4334-2021-2-08
23. Sukhova, O.V. Influence of the Structure and Cooling Rate of Fe–B–C Alloys on Mechanical Properties and Wear Resistance. *Metallofiz. Noveishie Tekhnol.* **2023**, *45*, 1337–1348. https://doi.org/10.15407/mfint.45.11.1337
24. Ulbrich, D.; Kowalczyk, J.; Jósko, M.; Sawczuk, W.; Chudyk, P. Assessment of Selected Properties of Varnish Coating of Motor Vehicles. *Coatings* **2021**, *11*, 1320. https://doi.org/10.3390/coatings11111320
25. Viňáš, J.; Brezinová, J.; Sailer, H.; Brezina, J.; Sahul, M.; Maruschak, P.; Prentkovskis, O. Properties Evaluation of the Welded Joints Made by Disk Laser. *Materials* **2021**, *14*, 2002. https://doi.org/10.3390/ma14082002

 doi:10.20944/preprints202606.0435.v1




26. Ulbrich, D.; Psuj, G.; Bartkowski, D.; Bartkowska, A. Assessment of Coating Properties in Car Body by Ultrasonic Method. *Appl. Sci.* **2024**, *14*, 8117. https://doi.org/10.3390/app14188117
27. Ratov, B.; Mechnik, V.A.; Rucki, M.; Hevorkian, E.; Bondarenko, N.; Prikhna, T.; Moshchil, V.E.; Kolodnitskyi, V.; Morozow, D.; Gusmanova, A.; Jerzy Jozwik, J,; Arshidinova, M.; Tofil, A. Enhancement of the Refractory Matrix Diamond-Reinforced Cutting Tool Composite with Zirconia Nano-Additive. *Materials* **2024**, *17*, 2852. https://doi.org/10.3390/ma17122852
28. Fekiač, J.J.; Krbata, M.; Kohutiar, M.; Janík, R.; Kakošová, L.; Breznická, A.; Eckert, M.; Mikuš, P. Comprehensive Review: Optimization of Epoxy Composites, Mechanical Properties, & Technological Trends. *Polymers* **2025**, *17*, 271. https://doi.org/10.3390/polym17030271
29. Blau, PJ. Wear Testing, Metals Handbook Desk Edition, 2nd ed. J.R. Davis, Ed., ASM International, 1998, 1342-1347
30. Holmberg, K.; Erdemir, A. Influence of Tribology on Global Energy Consumption, Costs and Emissions. *Friction*. **2017**, 5, 263-284. https://doi.org/10.1007/s40544-017-0183-5
31. Kozłowska, A.; Wojtacha, A. Advanced High-Strength Medium-Manganese Steels as an Alternative to Conventional Forging Steels: A Review. *Materials* **2026**, *19*, 109. https://doi.org/10.3390/ma19010109
32. Zhao, L.; Liu, H.; Chen, X.; Zhai, G.; Zhai, Q. Mechanical Properties and Impact Abrasive Wear Resistance in Vanadium Microalloyed Medium Carbon CrMo Cast Steel Strengthened with Nanoprecipitates. *Wear*, **2025**, *562*, 205679.
33. He, T.; Zhao, S.; Lu, D.; Jiang, Y.; Zhou, M. Abrasive Wear Performance of Spherical Hierarchical Structured TiC/High-Manganese Steel Composites. *Materials* **2025**, *18*, 130. https://doi.org/10.3390/ma18010130
34. Lencina, R.; Caletti, C.; Brunelli, K.; Micone, R. Assessing Wear Performance of Two High-carbon Hadfield Steels through Field Tests in the Mining Industry. *Procedia Mater Sci*, **2015**, 9, 358-366, https://doi.org10.1016/j.mspro.2015.05.005
35. Canadinc, D.; Sehitoglu, H.; Maier, H.J.; Chumlyakov, Y.I. Strain Hardening Behavior of Aluminum Alloyed Hadfield Steel Single Crystals. *Acta. Mater.*, **2005**, *53*, 1831-1842.
36. Idrissi, H.; Renard, K.; Ryelandt, L.; Schryvers, D.; Jacques, P.J. On the Mechanism of Twin Formation in Fe-Mn-C TWIP Steels. *Acta Mater*. **2010**, 58, 2464-2476. https://doi.org/10.1016/j.actamat.2009.12.032
37. Ge, S.; Wang, Q.; Wang, J. The impact Wear-Resistance Enhancement Mechanism of Medium Manganese Steel and its Applications in Mining Machines. *Wear*, **2017**, *376*, 1097-1104. https://doi.org/10.1016/j.wear.2017.01.015
38. Krbaťa, M.; Majerík, J.; Barényi, I.; Mikušová, I.; Kusmič, D. Mechanical and Tribological Features of the 90MnCrV8 Steel after Plasma Nitriding. *Manuf. Technol.* **2019**, *19*, 238–242.
39. Kozłowska, A.; Wojtacha, A. Advanced High-Strength Medium-Manganese Steels as an Alternative to Conventional Forging Steels: A Review. *Materials* **2026**, *19*, 109. https://doi.org/10.3390/ma19010109
40. Luo, Q.; Kitchen, M.; Li, J.; Li, W.; Li, Y. Experimental Investigation on the Spalling Failure of a Railway Turnout Made from Hadfield Steel. *Wear* **2023**, *523*, 204779. https://doi.org/10.1016/j.wear.2023.204779
41. Hu, B.; Luo, H.; Yang, F.; Dong, H. Recent Progress in Medium-Mn Steels Made with New Designing Strategies, a Review. *J. Mater. Sci. Technol.* **2017**, *33*, 1457–1464.
42. Kim, J.-K.; De Cooman, B.C. Stacking Fault Energy and Deformation Mechanisms in Fe-xMn-0.6C-yAl TWIP Steel. *Mater. Sci. Eng. A*, **2016**, 676, 216-231. https://doi.org/10.1016/j.msea.2016.08.106
43. Andrés, C.G.D.; Capdevila, C.; Martín, D.S.; Caballero, F.G. Effect of Titanium on the Allotriomorphic Ferrite Transformation Kinetics in Medium Carbon-Manganese Steels. *Mater. Sci. Eng. A*, **2002**, 328. 156-160
44. Wang, J.; Wang, Q.; Zhang, X.; Zhang, D. Impact and Rolling Abrasive Wear Behavior and Hardening Mechanism for Hot-Rolled Medium-Manganese Steel. *J. Tribol.* **2018**, *140*.
45. Yan, J.; Zhou, M.; Wu, H.; Liang, X.; Xing, Z.; Li, H.; Zhao, L.; Jiao, S.; Jiang, Z. A Review of Key Factors Affecting the Wear Performance of Medium Manganese Steels. *Metals* **2023**, *13*, 1152. https://doi.org/10.3390/met13071152
46. Huang,Q.; Liu, Z.; Hao, L.; Hu, T. Shot Blasting for Enhancing Wear Resistance and Impact Resistance of SCMnH11 High-Manganese Steel. *Metals* 2025, 15, 1179. https://doi.org/10.3390/met15111179

 doi:10.20944/preprints202606.0435.v1




47. Yan, J.; Zhou, M.; Wu, H.; Liang, X.; Xing, Z.; Li, H.; Zhao, L.; Jiao, S.; Jiang, Z. A Review of Key Factors Affecting the Wear Performance of Medium Manganese Steels. *Metals* **2023**, *13*, 1152. https://doi.org/10.3390/met13071152
48. He, Z.; Qi, C.; Fu, S.; Xie, J. Improved Work-hardening Ability and Wear Resistance of Austenitic Manganese Steel under Non-Severe Impact-Loading Conditions. *Wear* **1987**, 120, 305–319. https://doi.org/10.1016/0043-1648(87)90024-X
49. Chen, H.; Zhao, D.; Wang, Q.; Qiang, Y.; Qi, J. Effects of Impact Energy on the Wear Resistance and Work hardening Mechanism of Medium Manganese Austenitic Steel. *Friction* **2017**, 5, 447–454. https://doi.org/10.1007/s40544-017-0158-6
50. Zou, Y.; Xu, Y.B.; Hu, Z.P.; Gu, X.L.; Peng, F.; Tan, X.D.; Chen, S.Q.; Han, D.T.; Misra, R.D.K.; Wang, G.D. Austenite Stability and its Effect on the Toughness of a High Strength Ultra-Low Carbon Medium Manganese Steel Plate. *Mater. Sci. Eng. A* **2016**, *675*, 153–163. https://doi.org/10.1016/j.msea.2016.07.104
51. Yan, X.; Hu, J.; Yu, H.; Wang, C.; Xu, W. Unraveling the Significant Role of Retained Austenite on the Dry Sliding Wear Behavior of Medium Manganese Steel. *Wear* **2021**, *476*. https://doi.org/10.1016/j.wear.2021.203745
52. Xiong, R.; Peng, H.; Si, H.; Zhang, W.; Wen, Y. Thermodynamic Calculation of Stacking Fault Energy of the Fe–Mn–Si–C High Manganese Steels. *Mater. Sci. Eng. A*, **2014**, *598*, 376–86, https://doi.org/10.1016/j.msea.2014.01.046
53. Chen, A.Y.; Ruan, H.H.; Wang, J.; Chan, H.L.; Wang, Q.; Li, Q.; Lu, J. The Influence of Strain Rate on the Microstructure Transition of 304 Stainless Steel. *Acta Mater.* **2011**, 59, 3697–3709. https://doi.org/10.1016/j.actamat.2011.03.005
54. Mogilny, G.S.; Teus, S.M.; Shyvanyuk, V.N.; Gavriljuk, V.G. Plastic Deformation and Phase Transformations in Austenitic Steels in the Course of Hydrogen Charging and Subsequent Mechanical Tests. *Mater. Sci. Eng. A* **2015**, 648, 260-264. https://doi.org/10.1016/j.msea.2015.09.015
55. Teus, S.M.; Shyvanyuk, V.N.; Gavriljuk, V.G. Hydrogen-Induced γ→ ε Transformation and the Role of ε-Martensite in Hydrogen Embrittlement of Austenitic Steels. *Mater. Sci. Eng. A* **2008**, 497, 290-294. https://doi.org/10.1016/j.msea.2008.07.003
56. Vasylyev, M.A.; Mordyuk, B.N.; Sidorenko, S.I.; Voloshko, S.M.; Burmak, A.P. Influence of Microstructural Features and Deformation-Induced Martensite on Hardening of Stainless Steel by Cryogenic Ultrasonic Impact Treatment. *Surf. Coat. Technol.* **2018**, 343, 57-68. https://doi.org/10.1016/j.surfcoat.2017.11.019
57. De, A.K.; Murdock, D.C.; Mataya, M.C.; Speer, J.G.; Matlock, D.K. Quantitative Measurement of Deformation-Induced Martensite in 304 Stainless Steel by X-ray Diffraction, *Scripta Mater.* **2004**, 50, 1445–1449. https://doi.org/10.1016/j.scriptamat.2004.03.011
58. Jee, K.K.; Han, J.H.; Jang, W.Y. Measurement of Volume Fraction of ε Martensite in Fe–Mn Based Alloys. *Mater. Sci. Eng. A* **2004**, 378, 319–322. https://doi.org/10.1016/j.msea.2003.10.371
59. Kwok, T.W.J.; Gong, P.; Xu, X.; Nutter, J.; Rainforth, W.M.; Dye, D. Microstructure Evolution and Tensile Behaviour of a Cold Rolled 8 Wt Pct Mn Medium Manganese Steel. *Metal. Mater. Trans. A* **2022**, 53, 597–609. https://doi.org/10.1007/s11661-021-06534-9
60. Ma, Y. Medium-Manganese Steels Processed by Austenite-Reverted Transformation Annealing for Automotive Applications. *Mater. Sci. Technol.* **2017**, 33, 1713–1727. https://doi.org/10.1080/02670836.2017.1312208
61. Lee, S.; De Cooman, B.C. Tensile Behavior of Intercritically Annealed 10 pct Mn Multi-phase Steel. *Metall. Mater. Trans. A* **2013**, *45*, 709–716. https://doi.org/10.1007/s11661-013-2047-6
62. Lee, S.; Estrin, Y.; De Cooman, B.C. Effect of the Strain Rate on the TRIP–TWIP Transition in Austenitic Fe-12 pct Mn-0.6 pct C TWIP Steel. *Metall Mater Trans A* **2014**, 45, 717–730. https://doi.org/10.1007/s11661-013-2028-9
63. Koyama, M.; Sawaguchi, T. Overview of ε-Martensite-Related Damage Evolution and its Solution: Pathways for Local Stress Accommodation, Plastic Damage Retardation, and Microcrack Arrest. *ISIJ Int.* **2025**, *65*(4), 471-488. https://doi.org/10.2355/isijinternational.ISIJINT-2024-398

 doi:10.20944/preprints202606.0435.v1




64. Zou, Y.; Xu, Y.B.; Hu, Z.P.; Gu, X.L.; Peng, F.; Tan, X.D.; Chen, S.Q.; Han, D.T.; Misra, R.D.K.; Wang, G.D. Austenite Stability and its Effect on the Toughness of a High Strength Ultra-Low Carbon Medium Manganese Steel plate. *Mater. Sci. Eng. A* **2016**, *675*, 153–163.
65. Ojala, N.; Valtonen, K.; Heino, V.; Kallio, M.; Aaltonen, J.; Siitonen, P.; Kuokkala, V.-T. Effects of Composition and Microstructure on the Abrasive Wear Performance of Quenched Wear Resistant Steels. *Wear* **2014**, *317*, 225–232.
66. Stachowiak, A.; Wieczorek, A.N. Comparative Tribocorrosion Tests of 30CrMo12 Cast Steel and ADI Spheroidal Cast Iron. *Tribol. Int.* **2021**, *155*.
67. Rendón, J.; Olsson, M. Abrasive Wear Resistance of Some Commercial Abrasion Resistant Steels Evaluated by Laboratory Test Methods. *Wear* **2009**, *267*, 2055–2061.
68. Hokkirigawa, K.; Kato, K. An Experimental and Theoretical Investigation of Ploughing, Cutting and Wedge Formation During Abrasive Wear. *Tribol. Int.* **1988**, *21*, 51–57.
69. Yan, W.; Fang, L.; Zheng, Z.; Sun, K.; Xu, Y. Effect of Surface Nanocrystallization on Abrasive Wear Properties in Hadfield Steel. *Tribol. Int.* **2009**, *42*, 634–641. https://doi.org/10.1016/j.triboint.2008.08.012
70. Jia, Y.; Cai, Z.; Yuan, M.; Wang, S.; Ma, L. Influence of Shot-Peening Treatment on Wear Resistance of Medium Manganese Steel. *J. Mater. Res. Technol.* **2024**, *31*, 3703–3711.
71. Zhao, E.; Peng, Y.; Yang, H.; Dong, Y.; Zhu, C.; Liu, H. Ultrasonic Shock Strengthening and Wear Mechanism of High Manganese Steel. *China Surf. Eng.***2023**,*36(3)*, 152-159. https://doi.org/10.11933/j.issn.1007-9289.20220726001
72. Grosdidier, T.; Novelli, M. Recent Developments in the Application of Surface Mechanical Attrition Treatments for Improved Gradient Structures: Processing Parameters and Surface Reactivity. *Mater. Trans.* **2019**, *60*, 1344-1355. https://doi.org/10.2320/matertrans.MF201929.
73. Kim, J.G.; Moon, J.H.; Amanov, A.; Kim, H.S. Strength and Ductility Enhancement in the Gradient Structured Twinning-Induced Plasticity Steel by Ultrasonic Nanocrystalline Surface Modification. *Mater. Sci. Eng. A* **2019**, *739*, 105-108. https://doi.org/10.1016/j.msea.2018.10.045
74. Yildirim H.C., Marquis G.B. Fatigue Strength Improvement Factors for High Strength Steel Welded Joints Treated by High Frequency Mechanical Impact. *Int. J. Fatigue* **2012**, 44, 168–76. http://doi.org/10.1016/j.ijfatigue.2012.05.002
75. Knysh, V.V., Mordyuk, B.N., Solovei, S.O., Nyrkova, L.I., Gatsenko, O.S. Corrosion Fatigue Behaviour of Butt-Welded Joints of Steel S355: Effects of HFMI Treatment Applied at Manufacturing or Operating Stages. *Int. J. Fatigue* **2026**, 208, 109575. https://doi.org/10.1016/j.ijfatigue.2026.109575
76. Mordyuk, B.N.; Prokopenko, G.I. Ultrasonic Impact Peening for the Surface Properties' Management. *J. Sound Vibration* **2007**, 308, 855-866. https://doi.org/10.1016/j.jsv.2007.03.054
77. Mordyuk, B.N.; Prokopenko, G.I. Ultrasonic Impact Treatment — an Effective Method for Nanostructuring the Surface Layers in Metallic Materials, Handbook of Mechanical Nanostructuring (Ed. M. Aliofkhazraei) (WileyVCH Verlag: 2015), (2015), pp. 417–434. https://doi.org/10.1002/9783527674947.ch17
78. Meng, S.; Zhou, Y.; Shi, Z.; Xiao, J.; Lou, L.; Wang, D.; Zhao, S.; Yang, Q.; Deng, C.; Xing, X. Ultrasonic Impact Inducing Surface Magnetic Neutrality and Mechanical Enhancement in Medium-Mn Steels. *J Mater Sci & Technol*. **2026**, 273, 310–319. https://doi.org/10.1016/j.jmst.2026.03.035
79. Trembach, B., Mordyuk, B., Krbata, M., Skoryk, M., Volovodiuk, A., Reshetnyk, O., Zakiev, V., Kuravska, N., Balenko, O., Kovalyov, S., Kyravskyi, M., Salnyk O. Impact of HFMI-Induced Surface Hardening on the Wear Mechanisms of High-Manganese Steel Hardfacing. *J Manuf & Mater Process* **2026**, 10, 108. https://doi.org/10.3390/jmmp10030108
80. Perepletchikov E.F.; Ryabtsev I.A.; Vasil'ev V.G.; Khaintse Kh. Structure and Properties of High-Carbon High-Vanadium Alloys on the Iron Base for Hard Facing. *Metallovedenie I Termicheskaya Obrabotka Metallov* **2003**, 5, 36-40.
81. Kim, J.H.; Ko, K.H.; Noh, S.D.; Kim, G.G.; Kim, S.J. The Effect of Boron on the Abrasive Wear Behavior of Austenitic Fe-Based Hardfacing Alloys. *Wear* **2009**, *267*, 1415–1419. https://doi.org/10.1016/j.wear.2009.03.017

 doi:10.20944/preprints202606.0435.v1




82. Zong, L.; Guo, N.; Li, R.; Yu, H. Effect of B Content on Microstructure and Wear Resistance of Fe-3Ti-4C Hardfacing Alloys Produced by Plasma-Transferred Arc Welding. *Coatings* **2019**, *9*, 265. https://doi.org/10.3390/coatings9040265
83. Ryabtsev, I.O.; Babinets, A.A.; Lentyuhov, I.P. Control of the Formation of Metal Structure Surface with Flux-Cored Wires. *Mater. Sci.* **2024**, **60**, 298–305. https://doi.org/10.1007/s11003-025-00885-z
84. Pereplyotchikov, Y.F.; Ryabtsev, I.O.; Babinets, A.A.; Ryabtsev, I.I.; Lentugov, I.P. The Influence of Fractional Powder Composition on the Metal Structure Surfaced by the Plasma-Powder Method. *Mater. Sci.* **2025**, 60, 620–625. https://doi.org/10.1007/s11003-025-00928-5
85. Hvozdetskyi, V.M.; Student, M.M.; Zadorozhna, K.R.; Veselivska, H.H.; Markovych, S.I.; Mozola, N.Z. Mechanical Characteristics of Electric Arc coatings sputtered on St3 steel and D16 Aluminum Alloy. Mater. Sci. **2025**, *61*, 147–155 . https://doi.org/10.1007/s11003-025-00973-0
86. Luk'yanenko, A.G.; Hvozdetskyi, V.M.; Student, M.M.; Student, O.Z.; Lavrys S.M. Mozola, N.Z.; Thermodynamic analysis of the formation of chemical compounds reactions during arc spraying of coatings with cored wires. *Mater. Sci.* **2024**, *60*, 283–290 . https://doi.org/10.1007/s11003-025-00883-1
87. Lekatou, A.G.; Sarika, V.; Efremenko, B.; Chabak, Y.; Efremenko, V.; Petrišinec, I.; Emmanouilidou, S.; Tsirka, K. Effect of Laser Surface Melting on the Microstructure and Corrosion Resistance of Laser Powder Bed Fusion and Wrought Ti-6Al-4V Alloys. *Coatings* **2025**, *15*, 1285. https://doi.org/10.3390/coatings15111285
88. Chabak, Y.; Petryshynets, I.; Efremenko, V.; Golinskyi, M.; Shimizu, K.; Zurnadzhy, V.; Sili, I.; Halfa, H.; Efremenko, B.; Puchy, V. Investigations of Abrasive Wear Behaviour of Hybrid High-Boron Multi-Component Alloys: Effect of Boron and Carbon Contents by the Factorial Design Method. *Materials* **2023**, *16*, 2530. https://doi.org/10.3390/ma16062530
89. Coetsee, T.; De Bruin, F. Investigation of Copper as Collector Metal in Sodium-Oxide Fluxed Aluminothermic Reduction of Manganese Ore. *Crystals* **2026**, *16*, 50. https://doi.org/10.3390/cryst16010050
90. Bembenek, M.; Prysyazhnyuk, P.; Shihab, T.; Machnik, R.; Ivanov, O.; Ropyak, L. Microstructure and Wear Characterization of the Fe-Mo-B-C—Based Hardfacing Alloys Deposited by Flux-Cored Arc Welding. *Materials* **2022**, *15*, 5074. https://doi.org/10.3390/ma15145074
91. Singla, Y.K.; Maughan, M.R.; Arora, N.; Dwivedi, D.K. Enhancing the Wear Resistance of Iron-Based Alloys: A comprehensive Review of Alloying Element Effects. *J. Manuf. Processes*, **2024**, *120*, 135-160. https://doi.org/10.1016/j.jmapro.2024.04.038
92. Srikarun, B.; Oo, H.Z.; Muangjunburee, P. Influence of Different Welding Processes on Microstructure, Hardness, and Wear Behavior of Martensitic Hardfaced Cladding. *J. Mater. Eng. Perform.* **2021**, **30**, 8984–8995. https://doi.org/10.1007/s11665-021-06109-0
93. Coetsee, T.; De Bruin, F. Sodium-Oxide Fluxed Aluminothermic Reduction of Manganese Ore for a Circular Economy: Cr Collector Metal Application. *Sustain. Chem.* **2025**, *6*, 30. https://doi.org/10.3390/suschem6030030
94. Vlasov, A.F.; Makarenko, N.A.; Kushchiy, A.M. Using Exothermic Mixtures in Manual Arc Welding and Electroslag Processes. *Weld. Int.* **2017**, *31*(7),565–570. https://doi.org/10.1080/09507116.2017.1295561
95. Vlasov, A.F.; Makarenko, N.A. Special Features of Heating and Melting Electrodes with an Exothermic Mixture in the Coating. *Weld. Int.* **2016**, *30*(9), 717–722. https://doi.org/10.1080/09507116.2016.1143586
96. Vora, J.; Patel, V.K.; Srinivasan, S.; Chaudhari, R.; Pimenov, D.Y.; Giasin, K.; Sharma, S. Optimization of Activated Tungsten Inert Gas Welding Process Parameters Using Heat Transfer Search Algorithm: With Experimental Validation Using Case Studies. *Metals* **2021**, *11*, 981. https://doi.org/10.3390/met11060981
97. Binande, P.; Shahverdi, H.R.; Farnia, A. Study on the Effect of Flux Composition on the Melting Efficiency of A-TIG of AISI 316L Stainless Steel: Experimental and Analytical Approaches. *J. Mater. Res. Technol.* **2024**, *33*, 9092–9108. https://doi.org/10.1016/j.jmrt.2024.11.231
98. Ansari, M. S.; Amirthalingam, M.; Agarwal, G. Microstructural Characterisation of Multi-Pass Stellite-6 Hardfacings Developed by Pulsed GMAW Technique. *Surf. Coat. Technol.* **2026**, 133178. https://doi.org/10.1016/j.surfcoat.2026.133178

 doi:10.20944/preprints202606.0435.v1




99. Kannan, A.R.; Kumar, N.P.; Palguna, Y.; Shanmugam, N.S.; Jun, T.S. Interface Characteristics and Dry Sliding Wear Behaviour of Hardfaced Stellite 6 Overlays on ASTM A36 Structural Steel. *Results in Engineering*. 2026, 109584. https://doi.org/10.1016/j.rineng.2026.109584
100. Coetsee, T.; De Bruin, F. Gas-Phase Reactions in Nano-Strand Formation from Al-Fe-Ni Powder Reacted with $CaF_2$-$SiO_2$-$Al_2O_3$-MgO-MnO-$TiO_2$ Flux at 1350 °C: SEM Study and Diffusion Calculations. *Reactions* **2025**, *6*, 1. https://doi.org/10.3390/reactions6010001
101. Coetsee, T.; De Bruin, F. A Review of the Thermochemical Behaviour of Fluxes in Submerged Arc Welding: Modelling of Gas Phase Reactions. *Processes* **2023**, *11*, 658. https://doi.org/10.3390/pr11030658
102. Chen, A.; Zhang, Y.; Coetsee, T.; Kaldre, I.; Wang, C. Element Transfer Behaviors of Agglomerated CaF2-ZrO2 Fluxes in EH36-Shipbuilding Steel Subject to High-Heat Input Submerged Arc Welding. *Metall Mater Trans B* **2024**, 55, 3995–4000. https://doi.org/10.1007/s11663-024-03233-9
103. Vlasov, A.F.; Makarenko, N.A.; Kushchiy, A.M. Using exothermic mixtures in manual arc welding and electroslag processes. *Weld. Int.* **2017**, 31, 565–570.
104. Fagundes, J.G.; Moreno, A.M.; Ribeiro, P.H.; Arias, A.R.; Bracarense, A.Q. Formation of TiC by the application of Ti6Al4V machining chips as flux Compounds of Tubular Wires. *J. Physics. Conference series*. **2018**, *1126*, 012027. https://doi.org/10.1088/1742-6596/1126/1/012027
105. Zharikov, S.V.; Grin, A.G. Investigation of Slags in Surfacing with Exothermic Flux-Cored Wires. *Weld. Int.* **2015**, *29(5)*, 386–389. https://doi.org/10.1080/09507116.2014.934538
106. Kassov, V.; Berezshna, O.; Yermakova, S.; Turchanin, D.; Malyhina, S. Features of Heating and Melting of Powder Tape for Surfacing of Composite and Complex-Alloyed Alloys. *East Eur. J. Enterp. Technol.* **2025**, *2*(134), 60–67. https://doi.org/10.15587/1729-4061.2025.327904
107. Babinets, A.A.; Voron, M.M.; Schwab, S.L. Influence of the Granulometric Composition of Flux-Cored Wire on the Surfacing Stability and Structure of 50Kh2N2MFS Metal. *Mater. Sci.* **2026**, *61*.
108. Kassov, V.; Berezshna, O.; Yermakova, S.; Malyhina, S.; Turchanin, D. Determining Formation Features of a Wear-Resistant Layer Surfaced with Powder Tape. *Eastern-European Journal of Enterprise Technologies*, **2025**, *6*(1 (138), 6–15. https://doi.org/10.15587/1729-4061.2025.346696
109. Świerczyńska, A.; Varbai, B.; Pandey, C.; Fydrych, D. Exploring the Trends in Flux-Cored Arc Welding: Scientometric Analysis Approach. *Int. J. Adv. Manuf. Technol.* **2024**, *130*, 87–110.
110. Routray, S.; Swain, R.; Mohapatro, R.N. Toward a Greener Weld for Integrating Sustainability into Welding Practices. In *Advanced Welding Technologies*; Wiley: Hoboken, NJ, USA, **2025**; pp. 447–476.
111. Świerczyńska, A.; Bet, J.; Gorgol, M.; Wolski, A. Effect of Rewinding on Flux-Cored Welding Wires. *Int. J. Adv. Manuf. Technol.* **2026**, 142, 1299–1312. https://doi.org/10.1007/s00170-025-17140-z
112. Trembach, B.O.; Silchenko, Y.A.; Sukov, M.G.; Ratska, N.B.; Duriagina, Z.A.; Krasnoshapka, I.V.; Kabatskyi, O.V.; Rebrova, O.M. Development of a Model of Transition Element Factor of Alloying Elements of Self-Shielding Flux-Cored Powder Wire and Optimization of its Core Filler Composition. *Mater. Sci.* **2024**, *59*, 733–740. https://doi.org/10.1007/s11003-024-00834-2
113. Trembach, I.O.; Trembach, B.O.; Grin, A.G.; Luzhetskyy, R.Ya.; Brechko, V.O.; Zakovorotniy, O.Yu.; Balenko, O.I.; Molchanov, H.I.; Rebrova, O.M.; Kabatskyi, O.V. Application of a Complete Factorial Experiment for Optimization of the Filling Factor and Charge Density of Self-Shielding Flux-Cored Powder Wire. *Mater. Sci.* **2025**. 60, 445–452. https://doi.org/10.1007/s11003-025-00904-z
114. Trembach, B.; Balenko, O.; Davydov, V.; Brechko, V.; Trembach, I.; Kabatskyi, O. Prediction the Melting Characteristics of Self-Shielded Flux Cored arc Welding (FCAW-S) with Exothermic Addition (CuO-Al). In Proceedings of the IEEE 4th International Conference on Modern Electrical and Energy System (MEES), Kremenchuk, Ukraine, 20–23 October 2022; pp. 1–6.https://doi.org/10.1109/MEES58014.2022.10005657
115. Li, H.L.; Liu, D.; Guo, N.; Chena, H.; Dua, Y.P.; Feng, J.C. The Effect of Alumino-Thermic Addition on Underwater Wet Welding Process Stability. *J. Mater. Process. Technol* .**2017**, *245*, 149–156. http://dx.doi.org/10.1016/j.jmatprotec.2017.02.023
116. Wang, J.; Li, H.; Hu, C.; Wang, Z.; Han, K.; Liu, D.; Wang, J.; Zhu, Q. The Efficiency of Thermite-Assisted Underwater Wet Flux-Cored Arc Welding Process: Electrical Dependence, Microstructural Changes, and Mechanical Properties. *Metals* **2023**, *13*, 831. https://doi.org/10.3390/met13050831

 doi:10.20944/preprints202606.0435.v1




117. Trembach, B.; Trembach, I.; Grin, A.; Makarenko, N.; Babych, O.; Knyazev, S.; Musairova, Y.; Krbata, M.; Balenko, O.; Vorobiov, O.; et al. Study of the Effects of Hardfacing Modes Carried out by FCAW-S with Exothermic Addition of $MnO_2$-Al on Non-Metallic Inclusions, Grain Size, Microstructure and Mechanical Properties. *Eng.* **2025**, *6*, 125. https://doi.org/10.3390/eng6060125
118. Li, H.; Hu, C.; Hu, J.; Han, K.; Wang, Z.; Yang, R.; Liu, D. Underwater Wet Welding of High-Strength Low-Alloy Steel Using Self-Shielded Flux-Cored Wire with Highly Exothermic Al/CuO Mixture. *J. Mater. Process. Technol*. **2024**, *328*, 118404. https://doi.org/10.1016/j.jmatprotec.2024.118404
119. Trembach, B.; Silchenko, Y.; Balenko, O.; Hlachev, D.; Kulahin, K.; Heiko, H.; Bellorin-Herrera, O.; Khabosha, S.; Zakovorotnyi, O.; Trembach, I. Study of the Hardfacing Process Using Self-Shielding Flux-Cored Wire with an Exothermic Addition with a Combined Oxidizer of the Al-($CuO/Fe_2O_3$) System. *Int. J. Adv. Manuf. Technol.* **2024**,*134*, 309–335. https://doi.org/10.1007/s00170-025-15414-0
120. Trembach, B.; Trembach, I.; Grin, A.; Makarenko, N.; Rebrov, O.; Musairova, Y.; Kuravska, N.; Knyazev, S.; Krasnoshapka, I.; Kuravskyi, M.; Krykun, V.; Nedashkovskyi, A.; Panchenko, A. Optimisation of hardfacing conditions carried out by self-shielded flux-cored wire using combined Taguchi method and factorial design. *Int. J. Adv. Manuf. Technol.* **2025,** *140*, 1367–1408. https://doi.org/10.1007/s00170-025-16325-w
121. Trembach, B.; Trembach, I.; Maliuha, V.; Knyazev, S.; Krbata, M.; Kabatskyi, O.; Balenko, O.; Zarichniak, Y.; Brechka, M.; Mykhailo, B.; Khabosha, S.; Kniazieva, H. Study of Self-shielded flux-cored wire with exothermic additions CuO-Al on weld bead morphology, microstructure, and mechanical properties. *Int. J. Adv. Manuf. Technol.* **2025**, *137*, 4685–4711. https://doi.org/10.1007/s00170-025-15414-0
122. Trembach, B.; Grin, A.; Subbotina, V.; Vynar, V.; Knyazev, S.; Zakiev, V.; Kabatskyi, O. Effect of Exothermic Addition (CuO-Al) on the Structure, Mechanical Properties and Abrasive Wear Resistance of the Deposited Metal During Self-Shielded Flux-Cored Arc Welding. *Tribol. Ind.* **2021**, *43*, 452–464. https://doi.org/10.24874/ti.1104.05.21.07
123. Trembach, B.; Krbata, M.; Haibadulov, B.; Iokhov, O.; Tsebriuk, I.; Pomohaiev, I.; Korobkov, Y.; Neduzha, L. Optimisation of Elemental Transfer Efficiency in Fe-C-Cr-Ti-Cu Hardfacing by Self-Shielded Flux-Cored Wire: A Synergistic Taguchi–ANOVA–FD–PCA–GRA Approach. *Eng.* **2026**, *7*, 139. https://doi.org/10.3390/eng7030139
124. Trembach, B.; Dmitriiev, O.; Kulahin, K.; Balenko, O.; Maliuha, V.; Neduzha, L. Hybrid Optimization of Hardfacing Conditions and the Content of Exothermic Additions in the Core Filler During the Flux-Cored Arc Welding Process. *Eng.* **2026**, *7*, 23. https://doi.org/10.3390/eng7010023
125. Chenakin, S.P.; Mordyuk, B.M.; Khripta, N.I.; Malinin, V.Y. Ultrasonic Impact Treatment: Assessing the Process Energetics. *Metallofiz. Noveishie. Tekhnol.* **2023**, *45*, 1109–1123. https://doi.org/10.15407/mfint.45.09.1109
126. Chenakin, S.P.; Mordyuk, B.M.; Khripta, N.I. Surface Composition, Structure and Corrosion Properties of a ZrTiNb Alloy: Effect of Impact Treatment Energy. *Vacuum* **2023**, *210*, 111889. https://doi.org/10.1016/j.vacuum.2023.111889
127. Knysh, V.V.; Solovei, S.O.; Lobanov, L.M.; Mikhodui, O.L.; Volosevich, P.Y.; Lesyk, D.A.; Burmak, A.P.; Mordyuk, B.N. Synergetic Effects of Macro-and Microscopic Residual Stresses Induced by High-Frequency Mechanical Impact Post-weld Treatment on Fatigue Strength Enhancement of S335 Steel T-Weld. *J. Mater. Eng. Perform.* **2024**,*33*,7537–7551. https://doi.org/10.1007/s11665-024-09355-0
128. Lesyk, D.A.; Mordyuk, B.N.; Dzhemelinskyi, V.V.; Voloshko, S.M.; Burmak, A.P. Optimization of Ultrasonic Impact Treatment for Surface Finishing and Hardening of AISI O2 Tool Steel by Experimental Design. *J. Mater. Eng. Perform*. **2022**, *31*, 8567–8584. https://doi.org/10.1007/s11665-022-06861-x.
129. Langi, E.; Zhao, L.G.; Jamshidi, P.; Attallah, M.M.; Silberschmidt, V.V.; Willcock, H.; Vogt, F. Microstructural and Mechanical Characterization of Thin-Walled Tube Manufactured with Selective Laser Melting for Stent Application. *J. Mater. Eng. Perform.* **2021**, *30*, 696–710. https://doi.org/10.1007/s11665-020-05366-9.
130. Lesyk, D.A.; Martinez, S.; Mordyuk, B.N.; Dzhemelinskyi, V.V.; Lamikiz, A.; Prokopenko, G.I.; Iefimov, M.O.; Grinkevych, K.E. Combining Laser Transformation Hardening and Ultrasonic Impact Strain

 doi:10.20944/preprints202606.0435.v1



Hardening for Enhanced Wear Resistance of AISI 1045 Steel. *Wear* **2020**, *462-463*, 203494. https://doi.org/10.1016/j.wear.2020.203494

131. Bondar, V.Y.; Danilchenko, V.E.; Mazanko, V.F.; Filatov, O.V.; Iakovlev, V.E. Effect of Cyclic Martensitic γ – ε – γ Transformations on Diffusion Characteristics of Carbon in an Iron–Manganese Alloy. *Prog. Phys. Met.* **2018**, *19*, 70–94. https://doi.org/10.15407/ufm.19.01.070
132. Zakiev, I.; Storchak, M.; Gogotsi, G.A.; Zakiev, V.; Kokoieva, Y. Instrumented Indentation Study of Materials Edge Chipping. *Ceramics Int.* **2021**, 47, 29638–29645. https://doi.org/10.1016/j.ceramint.2021.07.133
133. Storchak M.; Zakiev I.; Zakiev V.; Manokhin A. Coatings Strength Evaluation of Cutting Inserts Using Advanced Multi-Pass Scratch Method. *Measurement: J. Int. Measurement Confederation*, **2022**, 191, 110745. HTTPS://DOI.ORG/10.1016/j.measurement.2022.110745
134. Zakiev, V.; Nadtoka, V.; Zakiev, I.; Mordyuk, B.; Yakushenko, O.; Trofimov, I.; Skoryk, M.; Yutskevych, S. Micromechanical Properties and Tribological Performance of Mo, Cr, and Ta Coatings Obtained by Cathodic Arc-Deposition. *Coatings* **2025**, 15(3), 358. https://doi.org/10.3390/coatings15030358
135. Mechnik V.A.; Bondarenko N.A.; Kolodnitskyi V.M.; Zakiev V.I.; Zakiev I.M., Gevorkyan E.S., Kuzin N.O., Yakushenko O.S., Semak I.V. Comparative Study of the Mechanical and Tribological Characteristics of Fe–Cu–Ni–Sn Composites with Different CrB2 Content under Dry and Wet Friction. *J. Superhard Mater.* **2021**, 43, 52 – 64. HTTPS://DOI.ORG/10.3103/S1063457621010044
136. Zakiev, V.; Markovsky, A.; Aznakayev, E.; Zakiev, I.; Gursky, E. Micro-Mechanical Properties of Bio-Materials. Proc. SPIE 5959, Medical Imaging, 595916 (23 September 2005); https://doi.org/10.1117/12.628396
137. Zakiev, I.; Gogotsi, G.A.; Storchak, M.; Zakiev, V. Glass Fracture During Micro-Scratching. Surfaces, **2020**, 3, 211–224. https://doi.org/10.3390/surfaces3020016
138. Lozynskyi, V.; Trembach, B.; Hossain, M.M.; Kabir, M.H.; Silchenko, Y.; Krbata, M.; Sadovyi, K.; Kolomiitse, O.; Ropyak, L. Prediction of Phase Composition and Mechanical Properties Fe–Cr–C–B–Ti–Cu Hardfacing Alloys: Modeling and Experimental Validations. *Heliyon* **2024**, *10*,e26199.https://doi.org/10.1016/J.HELIYON.2024.E26199
139. Ball, A. On the Importance of Work Hardenning in the Design of Wear-Resistant Materials. *Wear* **1983**, *91*, 201–207
140. Xu, X.; van der Zwaag, S.; Xu, W. The Effect of Martensite Volume Fraction on the Scratch and Abrasion Resistance of a Ferrite–Martensite Dual Phase Steel. Wear, **2016**, 348, 80-88. https://doi.org/10.1016/j.wear.2015.11.017
141. Xu, X.; Ederveen, F.H.; van der Zwaag, S.; Xu, W. Correlating the Abrasion Resistance of Low Alloy Steels to the Standard Mechanical Properties: A Statistical Analysis Over a Larger Data Set. *Wear* **2016**, *368*, 92–100. http://dx.doi.org/10.1016/j.wear.2016.09.014
142. Qiao, Y.; Zhang, Z.-X.; Zhang, S. An Experimental Study of the Relation between Mode I Fracture Toughness, $K_{Ic}$, and Critical Energy Release Rate, $G_{Ic}$. *Materials* **2023**, *16*, 1056. https://doi.org/10.3390/ma16031056
143. Griffith, A.A. The Phenomena of Rupture and Flow in Solids. *Philos. Trans. R. Soc. Lond. Ser. A* **1921**, *221*, 163–198.
144. Irwin, G.R. Analysis of Stresses and Strains Near the End of a Crack Traversing a Plate. *J. Appl. Mech.* **1957**, *24*, 361–364.
145. Efstathiou, C.; Sehitoglu, H. Strain Hardening and Heterogeneous Deformation During Twinning in Hadfield Steel. *Acta Mater.* **2010**, *58*, 1479–1488.
146. Bei, H.; George, E. P.; Hay, J. L.; Pharr, G. M. Influence of Indenter Tip Geometry on Elastic Deformation During Nanoindentation. *Phys. Rev. Lett.* **2005**, *95*(4), 045501. https://doi.org/10.1103/PhysRevLett.95.045501
147. He, B.B.; Huang, M.X.; Liang, Z.Y.; Ngan, A.H.W.; Luo, H.W.; Shi, J.; Cao, W.Q.; Dong, H. Nanoindentation Investigation on the Mechanical Stability of Individual Austenite Grains in a Medium-Mn Transformation-Induced Plasticity Steel. *Scr. Mater.* **2013**, *69*, 215–218. https://doi.org/10.1016/j.scriptamat.2013.03.030
148. Ahn, T.H.; Lee, S.B.; Park, K.T.; Oh, K.H.; Han, H.N. Strain-Induced ε-Martensite Transformation during Nanoindentation of High-Nitrogen Steel. *Mater. Sci. Eng. A*, **2014**, *598*, 56-61. https://doi.org/10.1016/j.msea.2014.01.030

 doi:10.20944/preprints202606.0435.v1




149. Weidner, A.; Hangen, U.D.; Biermann, H. Nanoindentation Measurements on Deformation-Induced α-Martensite in a Metastable Austenitic High-Alloy CrMnNi Steel. *Philos. Mag. Lett.* **2014**, *94*, 522–530. https://doi.org/10.1080/09500839.2014.941027
150. Finkin, E.F. Examination of Abrasion Resistance Criteria for Some Ductile Metals. *J. Lubr. Technol*. **1974**, 96, 210-214. https://doi.org/10.1115/1.3451924
151. Leyland, A.; Matthews, A. On the Significance of the H/E Ratio in Wear Control: A Nanocomposite Coating Approach to Optimised Tribological Behaviour. *Wear* **2000**, 246, 1-11. https://doi.org/10.1016/S0043-1648(00)00488-9
152. Ratov, B.; Mechnik, V.; Hevorkian, E.; Rucki, M.; Pieniak, D.; Bondarenko, M.; Kolodnitskyi, V.; Starik, S.; Chishkala, V.; Kuttybaev, A.; Akhmedyanova, G.; Abilakhanova, A. Properties of WC-Co Cemented Carbide Reinforced with Yttria-Stabilized Zirconia Nanoparticles. *J. Compos. Sci.* **2026**, *10*, 156. https://doi.org/10.3390/jcs10030156
153. Cheng, B.; Wei, F.; Teh, W.H.; Cheong, K.H.; Lee, J.J.; Chew, L.T.; Lau, K.B.; Ma, T.H.B.; Ng, C.K.; Wang, P.; Ramamurty, U.; Tan, C.C. High Strength Hadfield Steel Produced Using Laser Powder Bed Fusion of Mixed Powders. *Mater. Design*, **2023**, *231*, 112017. https://doi.org/10.1016/j.matdes.2023.112017
154. Li, X.; Chen, L.; Zhao, Y.; Misra, R.D.K. Influence of Manganese Content on ε-/α′-Martensitic Transformation and Tensile Properties of Low-C high-Mn TRIP Steels. *Mater. Des.* **2018**, *142*, 190–202. https://doi.org/10.1016/j.matdes.2018.01.026
155. Otto, M.; Freudenberger, J.; Giebeler, L.; Weidner, A.; Hufenbach, J. Developing Austenitic High-Manganese High-Carbon Steels for Biodegradable Stent Applications: Microstructural and Mechanical Studies. *Mat. Sci. Eng. A* **2024**, *892*, 145998. https://doi.org/10.1016/j.msea.2023.145998
156. Mordyuk, B.N.; Milman, Y.V.; Iefimov, M.O.; Prokopenko, G.I.; Silberschmidt, V.V.; Danylenko, M.I.; Kotko, A.V. Characterization of ultrasonically peened and laser-shock peened surface layers of AISI 321 stainless steel. Surf. *Coat. Technol.* **2008**, 202, 4875–4883. https://doi.org/10.1016/j.surfcoat.2008.04.080
157. Paterson, M.S. X-ray Diffraction by Face-Centered Cubic Crystals with Deformation Faults, *J. Appl. Phys*. 1952, 23, 805. https://doi.org/10.1063/1.1702312
158. Jee, K.K.; Han, J.H.; Jang, W.Y. Measurement of Volume Fraction of ε Martensite in Fe–Mn Based Alloys. *Mater. Sci. Eng. A* **2004**, 378, 319–322. https://doi.org/10.1016/j.msea.2003.10.371
159. Kwok, T.W.J.; Gong, P.; Xu, X.; Nutter, J.; Rainforth, W.M.; Dye, D. Microstructure Evolution and Tensile Behaviour of a Cold Rolled 8 Wt Pct Mn Medium Manganese Steel. *Metal. Mater. Trans. A* **2022**, 53, 597–609. https://doi.org/10.1007/s11661-021-06534-9
160. Vinogradov, A. Fatigue Limit and Crack Growth in Ultra-fine Grain Metals Produced by Severe Plastic Deformation. *J. Mater. Sci.* **2007**, 42, 1797–1808. https://doi.org/10.1007/s10853-006-0973-z
161. Ye, C.; Suslov, S.; Lin, D.; Cheng, G.J. Deformation-Induced Martensite and Nanotwins by Cryogenic Laser Shock Peening of AISI 304 Stainless Steel and the Effects on Mechanical Properties. *Phil. Mag.* **2012**, *92*, 1369–1389. https://doi.org/10.1080/14786435.2011.645899
162. Zhang, D.; Du, X.; Liu, Y.; Sun, H.; Zheng, Y.; Yang, S.; Ma, C.; Wang, B. Construction and Regulation of Heterogeneous Structure in Medium Mn Steel with Critical Annealing–Quenching and Partitioning Process. *Mater. Design*, **2025**, *253*, 113941. https://doi.org/10.1016/j.matdes.2025.113941
163. Lai, Q.Q.; Song, P.F.; Zhou, H.; Xiao, L.R.; Feng, T.; Li, C.J. Deformation-Induced Martensitic Transformation and Strain Hardening in a Nanocrystalline FeMn Alloy Processed by Severe Austenite Pre-deformation. *Materialia* **2020**, 13, 100832. https://doi.org/10.1016/j.mtla.2020.100832
164. Figueiredo, R.B.; Sicupira, F.L.; Malheiros, L.R.C.; Kawasaki, M.; Santos, D.B.; Langdon, T.G. Formation of Epsilon Martensite by High-Pressure Torsion in a TRIP Steel. *Mater. Sci. Eng. A*, **2015**, *625*, 114-118. https://doi.org/10.1016/j.msea.2014.11.091
165. Wang, Z.B.; Tao, N.R.; Li, S.; Wang, W.; Liu, G.; Lu, J.; Lu, K. Effect of Surface Nanocrystallization on Friction and Wear Properties in Low Carbon Steel. *Mater. Sci. Eng. A* **2003**, 352, 144-149. https://doi.org/10.1016/S0921-5093(02)00870-5
166. Zhou, L.; Liu, G.; Han, Z.; Lu, K. Grain Size Effect on Wear Resistance of a Nanostructured AISI52100 steel. *Scripta Mater.* **2008**, 58, 445–448. 10.1016/j.scriptamat.2007.10.034

 doi:10.20944/preprints202606.0435.v1




167. Petrov, Y.N.; Gavriljuk, V.G.; Berns, H.; Schmalt, F. Surface Structure of Stainless and Hadfield Steel after Impact Wear. *Wear* **2006**, *260*, 687–691. https://doi.org/10.1016/j.wear.2005.04.009
168. Khoma, M.S.; Vynar, V.A.; Vasyliv, Ch.B.; Zakiev, V.I.; Datsko, B.M.; Golovchuk, M.Ya. Influence of Heat Treatment of 30MnB5 Steel on its Micromechanical Properties and Resistance to Abrasion Wear. *Tribology in Industry*. **2022**, 44, 310–321. https://doi.org/10.24874/ti.1146.06.21.02
169. Yanchuk, V.; Kruhlov, I.; Zakiev, V.; Lozova, A.; Trembach, B.; Orlov, A.; Voloshko, S. Thermal and Ion Treatment Effect on Nanoscale Thin Films Scratch Resistance. *Metallofiz Noveishie Tekhnol*. 2022, 44, 1275–1292. https://doi.org/10.15407/mfint.44.10.1275
170. Ignatovich S.R.; Zakiev I.M.; Borisov D.I.; Zakiev V.I. Material Surface Layer Damage Estimation for Cyclic Loading Conditions Using the Nanoindenting and Nanoscratching Techniques. *Strength Mater*. **2006**, 38, 428–434. https://doi.org/10.1007/s11223-006-0061-2
171. Feng, X.; Zhang, F.; Yang, Z.; Zhang, M. Wear Behaviour of Nanocrystallised Hadfield Steel. *Wear* **2013**, *305(1/2)*, 299-304. https://doi.org/10.1016/j.wear.2012.11.038
172. Kato, K.; Adachi, K. Wear mechanisms, in: B. Bhushan (Ed.), Modern Tribology Handbook, Taylor & Francis, CRC Press, 2000.
173. Yang, D.; Zhang, N.; Liu, Z.; Jiang, B. Defect Analysis of Surface Cracks in Mn18Cr2 High-Manganese Wear-Resistant Steel Plate. *Materials* **2026**, *19*, 241. https://doi.org/10.3390/ma19020241